

1 **Rheologic constraints on the upper mantle from five years of**
2 **postseismic deformation following the El Mayor-Cucapah**
3 **earthquake**

4 **T. T. Hines¹, E. A. Hetland¹**

5 ¹Department of Earth and Environmental Sciences, University of Michigan, Ann Arbor, Michigan, USA.

6 **Key Points:**

- 7 • Transient postseismic deformation can be observed following the El Mayor-Cucapah
8 earthquake at epicentral distances of up to 400 km
9 • Near-field postseismic deformation exhibits early transience that decays to a sustained
10 rate which is elevated above the preseismic trend
11 • ~~A Far-field postseismic deformation can be explained with a Zener or Burgers upper~~
12 ~~mantle can explain far-field deformation while near-field transience can be described~~
13 ~~with afterslip rheology upper mantle~~

14 **Abstract**

15 ~~Five years of postseismic deformation following the Mw7.2~~ We analyze five years of Southern
 16 California GPS data following the ~~Mw=7.2~~ El Mayor-Cucapah earthquake ~~reveals transient deformation~~
 17 ~~that decays back to its pre-earthquake trend after about~~. We observed transient postseismic
 18 deformation which persists ~~for~~ three years at epicentral distances greater than ~ 200 km. At
 19 ~~closer distances, the rapid~~ In the near-field, rapid postseismic transience decays to a sustained
 20 rate which exceeds its ~~pre-earthquake~~ preseismic trend. We attempt to determine the mech-
 21 anisms driving this deformation, where we consider afterslip at seismogenic depths and vis-
 22 coelastic relaxation in the lower crust and upper mantle as candidate mechanisms. We find that
 23 early, rapid, near-field deformation can be explained with afterslip on the fault that ruptured
 24 coseismically, while the later, sustained, near-field deformation can be explained with either
 25 continued afterslip in an effectively elastic lower crust, or lower crustal viscoelastic relaxation
 26 with a steady-state viscosity of $\sim 10^{19}$ Pa s. The trend in far-field deformation is best explained
 27 with a transient viscosity of $\sim 10^{18}$ Pa s in the upper mantle. We argue that a transient rhe-
 28 ology in the mantle is preferable over a Maxwell rheology because it better predicts the de-
 29 cay in postseismic deformation, and also because it does not conflict with the generally higher,
 30 steady-state viscosities inferred from studies of geophysical processes occurring over longer
 31 time-scales.

32 **1 Introduction**

33 Ground deformation in the years following a large (~~Mw>Mw7~~) ~~earthquake provides~~ 7
 34 ~~earthquake can be used to gain~~ insight into the mechanical behavior of the crust and upper man-
 35 ~~tle. It has long been recognized that~~ The interpretations of postseismic deformation ~~can be ambiguous~~
 36 ~~are not always conclusive~~ because multiple postseismic deformation mechanisms, such as afterslip
 37 ~~or viscoelastic relaxation in the lower crust and upper mantle~~, can have qualitatively similar
 38 surface expressions [e.g. Savage, 1990]. This non-uniqueness complication can potentially be
 39 remedied if the postseismic deformation occurs in an area that is sufficiently well instrumented
 40 with GPS stations [Hearn, 2003]. Owing to the dense geodetic network deployed through-
 41 out the 2000s as part of the Plate Boundary Observatory, the postseismic deformation follow-
 42 ing the April 4, 2010, ~~Mw7.2~~ ~~Mw=7.2~~ El Mayor-Cucapah earthquake in Baja California was
 43 observed at more GPS stations than any other earthquake in California to date (see Hauksson *et al.* [2011] and
 44 Fletcher *et al.* [2014] for a detailed description of this earthquake and its seismotectonic context).
 45 With such a large collection of data, we attempt to discern the mechanisms driving ~~postseismic~~
 46 ~~deformation following the El Mayor-Cucapah earthquake, where we consider both afterslip~~
 47 ~~and viscoelastic relaxation in the lower crust and upper mantle as candidate mechanisms~~ the
 48 ~~postseismic deformation~~.

49 Previous studies which have modeled postseismic deformation following the El Mayor-
 50 Cucapah earthquake include Pollitz *et al.* [2012], Gonzalez-Ortega *et al.* [2014], Spinler *et al.*
 51 [2015], and Rollins *et al.* [2015]. Of these studies, Gonzalez-Ortega *et al.* [2014] and Rollins
 52 *et al.* [2015] have attempted to describe the postseismic deformation with afterslip in an elas-
 53 tic half-space. Gonzalez-Ortega *et al.* [2014] described five months of postseismic deforma-
 54 tion, observed by InSAR and GPS ~~stations~~ within ~ 50 km of the rupture, with afterslip and
 55 contraction on the coseismically ruptured fault. Gonzalez-Ortega *et al.* [2014] noted that their
 56 preferred model underestimated the GPS displacements for stations $\gtrsim 25$ km from the rup-
 57 ture and suggested that it could be the result of unmodeled viscoelastic relaxation. Using only
 58 continuous GPS stations, which are mostly north of the rupture zone, Rollins *et al.* [2015] found
 59 that three years of postseismic deformation can be adequately explained by afterslip, albeit with
 60 an implausibly large amount of slip inferred on the least constrained, southern-most fault seg-
 61 ment. Here, we suggest the afterslip inferred by Rollins *et al.* [2015] may have been acting as
 62 a proxy for distributed relaxation in the upper mantle.

63 Pollitz *et al.* [2012], Rollins *et al.* [2015] and Spinler *et al.* [2015] have explored viscoelas-
 64 tic relaxation in the lower crust and upper mantle as a potential postseismic deformation mech-

anism. The rheology of the crust and mantle is largely unknown and so modeling postseismic deformation with viscoelastic relaxation requires one to assume a rheologic model and then find the best fitting rheologic parameters. The inference of these rheologic parameters is a computationally expensive non-linear inverse problem which is typically approached with a forward modeling grid search method. Consequently, a simplified structure for the Earth must be assumed in order to minimize the number of rheologic parameters that need to be estimated. For example, it is commonly assumed that the lower crust and upper mantle are homogeneous, Maxwell viscoelastic layers, which may be too simplistic for postseismic studies [Riva and Govers, 2009; Hines and Hetland, 2013]. To further reduce the dimensions of the model space, it is also necessary to make simplifying assumptions about the ~~nature~~behavior of afterslip. For example, one can assume a frictional model for afterslip and parametrize afterslip in terms of the unknown rheologic properties of the fault [e.g. Johnson *et al.*, 2009; Johnson and Segall, 2004]. One can also assume that afterslip does not persist for more than a few months and then model the later postseismic deformation assuming it to be the result of only viscoelastic relaxation [e.g. Pollitz *et al.*, 2012; Spinler *et al.*, 2015]. However, ~~postseismic~~-afterslip in similar tectonic settings has been observed to persist for decades following earthquakes [Çakir *et al.*, 2012; Cetin *et al.*, 2014]. Indeed, the preferred viscoelastic model from Pollitz *et al.* [2012] significantly underestimates deformation in the Imperial Valley, which could be indicative of unmodeled continued afterslip. Neglecting to allow for sustained afterslip as a postseismic mechanism could then lead to biased inferences of viscosities.

In this study, we perform a kinematic inversion for fault slip, allowing it to persist throughout the postseismic period, while simultaneously estimating the viscosity of the lower crust and upper mantle. We create an initial model of the fault slip and effective viscosity necessary to describe early postseismic deformation using the method described in Hines and Hetland [2016]. This method ~~utilizes~~uses a first-order approximation of surface deformation resulting from viscoelastic relaxation which is only applicable to the early postseismic period. In this case, our initial model describes the first 0.8 years of postseismic deformation following the El Mayor-Cucapah earthquake. We then use the inferred effective viscosity structure from the initial model to create a suite of postseismic models to explain the five years of postseismic data available to date. Of the suite of models tested, we find that postseismic deformation following the El Mayor-Cucapah earthquake can be explained with a combination of afterslip on a fault segment running through the Sierra Cucapah and ~~viscoelastic relaxation in~~ a Zener rheology ~~in the~~ upper mantle with a transient viscosity ~~that decays from 6×10^{18} Pa s to 1×10^{18} Pa s at 120 km depth~~on the order of 10^{18} Pa s.

106 2 Data Processing

We use continuous GPS position time series provided by University Navstar Consortium (UNAVCO) for stations within a 400 km radius about the El Mayor-Cucapah epicenter. We collectively describe the coseismic and postseismic displacements resulting from the El Mayor-Cucapah earthquake as $u_{\text{post}}(t)$. We consider the GPS position time series, $u_{\text{obs}}(t)$, to be the combination of $u_{\text{post}}(t)$, secular tectonic deformation, annual and semi-annual oscillations, and coseismic offsets from significant earthquakes over the time span of this study. The June 14, 2010, ~~Mw5.8~~Mw=5.8 Ocotillo earthquake and the Brawley swarm, which included an ~~Mw5.5~~Mw=5.5 and an ~~Mw5.4~~Mw=5.4 event on August 26, 2012 (Figure 1), are the only earthquakes that produced noticeable displacements in any of the time series. We treat the displacements resulting from the Brawley swarm as a single event because the daily solutions provided by UNAVCO cannot resolve the separate events. Although the Ocotillo earthquake had its own series of aftershocks [Hauksson *et al.*, 2011], neither the Ocotillo earthquake nor the Brawley swarm produced detectable postseismic deformation. We model displacements resulting from these events with only a Heaviside function, $H(t)$, describing the coseismic offsets. We then model $u_{\text{obs}}(t)$ as

$$u_{\text{obs}}(t) = u_{\text{pred}}(t) + \epsilon, \quad (1)$$

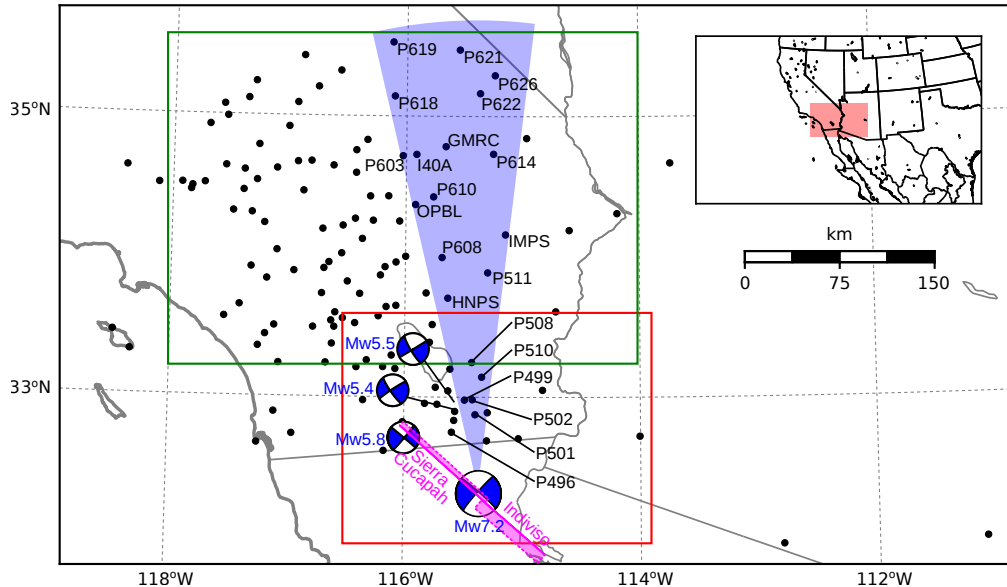


Figure 1. Map of the region considered in this study. The large focal mechanism is [the GCMT solution](#) for the El Mayor-Cucapah earthquake, and the three small focal mechanisms are for the Ocotillo earthquake and the two main shocks during the Brawley swarm. The black dots indicate the locations of GPS stations used in this study. The fault geometry used in this study is shown in [cyan-magenta](#) where dashed lines indicate buried edges of the fault segments. The green and red boxes demarcate the extent of the near-field and far-field maps (Figures 4 and 5). Stations inside the blue sector, which highlights the area within 10° of the El Mayor-Cucapah [P-axis](#), are used in Figures ??, 10, ?? and ??.

where

$$u_{\text{pred}}(t) = u_{\text{post}}(t)H(t - t_{\text{emc}}) + c_0 + c_1t + c_2 \sin(2\pi t) + c_3 \cos(2\pi t) + c_4 \sin(4\pi t) + c_5 \cos(4\pi t) + c_6 H(t - t_{\text{oc}}) + c_7 H(t - t_{\text{bs}}). \quad (2)$$

In the above equations, t_{emc} , t_{oc} and t_{bs} are the times of the El Mayor-Cucapah earthquake, Ocotillo earthquake, and the Brawley swarm, respectively, c_0 through c_7 are unknown coefficients, and ϵ is the observation noise. We are using years as our unit of time which makes c_2 through c_5 the coefficients for annual and semi-annual oscillations. We only estimate jumps associated with the Ocotillo earthquake and Brawley swarm for stations within 40 km of their epicenters.

Stations which recorded displacements that clearly cannot be described by the aforementioned processes are not included in our analysis. This includes stations in the Los Angeles basin, where anthropogenic deformation can be larger than the postseismic signal that we are trying to estimate [Bawden *et al.*, 2001; Argus *et al.*, 2005]. In order to ensure an accurate estimation of the secular deformation, we only use stations that were installed at least six months prior to El Mayor-Cucapah earthquake ~~Several even though several~~ GPS stations were installed after the ~~El Mayor-Cucapah earthquake to improve the spatial resolution of postseismic deformation [Spinler *et al.*, 2015]~~. ~~Although it~~ ~~earthquake to get better coverage of the postseismic deformation field [Spinler *et al.*, 2015]~~. It would be possible to subtract secular velocities derived from elastic block models [e.g. Meade and Hager, 2005] from velocities recorded at the newly installed stations to get an estimate of postseismic velocities ~~, we do not do so here. We use coseismic and postseismic displacements, rather than velocities, in our inverse method described~~

141 ~~in Section 3. We use displacements because at those stations. However,~~ estimating velocities
 142 from an already noisy displacement time series can introduce significant uncertainties depend-
 143 ing on exactly how the estimation is done. ~~We therefore use coseismic and postseismic displacements,~~
 144 ~~rather than velocities, in our inverse method described in Section 3.~~ This choice prevents us
 145 from using the newly installed stations ~~in Baja California~~ for our analysis.

146 The October 16, 1999, ~~Mw7.1~~ ~~Mw=7.1~~ Hector Mine earthquake, which occurred \sim 270
 147 km north of the El Mayor-Cucapah epicenter, produced transient postseismic deformation which
 148 we do not wish to model, either mechanically or through empirical line fitting. We thus re-
 149 strict our analysis to deformation observed six years after the Hector Mine earthquake, which
 150 is when postseismic velocities at sites ~~proximal-to-near~~ the Hector Mine epicenter are approx-
 151 imately constant [Savage and Svart, 2009]. When appraising our model fit in Section 3, we
 152 see some systematic residuals in the vicinity of the Hector Mine epicenter, which may be the
 153 result of errors in the assumption that the trend in Hector Mine postseismic deformation is lin-
 154 ear after six years.

155 Studies of postseismic deformation typically assume a parametric form for $u_{\text{post}}(t)$, such
 156 as one with a logarithmic or exponential time dependence [e.g. Savage *et al.*, 2005]. However,
 157 by assuming a logarithmic or exponential form of $u_{\text{post}}(t)$ we run the risk of over fitting the
 158 GPS time series and inferring a non-existent postseismic signal. We therefore do not assume
 159 any parametric form for $u_{\text{post}}(t)$ and rather treat it as integrated Brownian motion, so that

$$\dot{u}_{\text{post}}(t) = \sigma^2 \int_0^t w(s) ds, \quad (3)$$

160 where $w(t)$ is white noise and the variance of $\dot{u}_{\text{post}}(t)$ increases linearly with time by a fac-
 161 tor of σ^2 . We use a Kalman filtering approach to estimate $u_{\text{post}}(t)$ and the unknown param-
 162 eters in eq. (2). In the context of Kalman filtering, our time varying state vector is

$$\mathbf{X}(t) = [u_{\text{post}}(t), \dot{u}_{\text{post}}(t), c_0, \dots, c_7] \quad (4)$$

163 and eq. (2) is the observation function which maps the state vector to the GPS observations.
 164 We initiate the Kalman filter by assuming a prior estimate of $\mathbf{X}(t)$ at the first time epoch, de-
 165 noted $\mathbf{X}_{1|0}$, which has a sufficiently large covariance, denoted $\Sigma_{1|0}$, to effectively make our
 166 prior uninformed. For each time epoch t_i , Bayesian linear regression is used to incorporate
 167 GPS derived estimates of displacement with our prior estimate of the state $\mathbf{X}_{i|i-1}$ to form
 168 a posterior estimate of the state $\mathbf{X}_{i|i}$, which has covariance $\Sigma_{i|i}$. We then use the posterior
 169 estimate of the state at time t_i to form a prior estimate of the state at time t_{i+1} through the
 170 transition function

$$\mathbf{X}_{i+1|i} = \mathbf{F}_{i+1} \mathbf{X}_{i|i} + \delta_{i+1}, \quad (5)$$

171 where

$$\mathbf{F}_{i+1} = \begin{bmatrix} 1 & (t_{i+1} - t_i) & \mathbf{0} \\ 0 & 1 & \mathbf{0} \\ \mathbf{0} & \mathbf{0} & \mathbf{I} \end{bmatrix} \quad (6)$$

172 and δ_{i+1} is the process noise, which has zero mean and covariance described by

$$\mathbf{Q}_{i+1} = \sigma^2 \begin{bmatrix} \frac{(t_{i+1} - t_i)^3}{3} & \frac{(t_{i+1} - t_i)^2}{2} & \mathbf{0} \\ \frac{(t_{i+1} - t_i)^2}{2} & (t_{i+1} - t_i) & \mathbf{0} \\ \mathbf{0} & \mathbf{0} & \mathbf{0} \end{bmatrix}. \quad (7)$$

173 The covariance of the new prior state, $\mathbf{X}_{i+1|i}$, is then described by

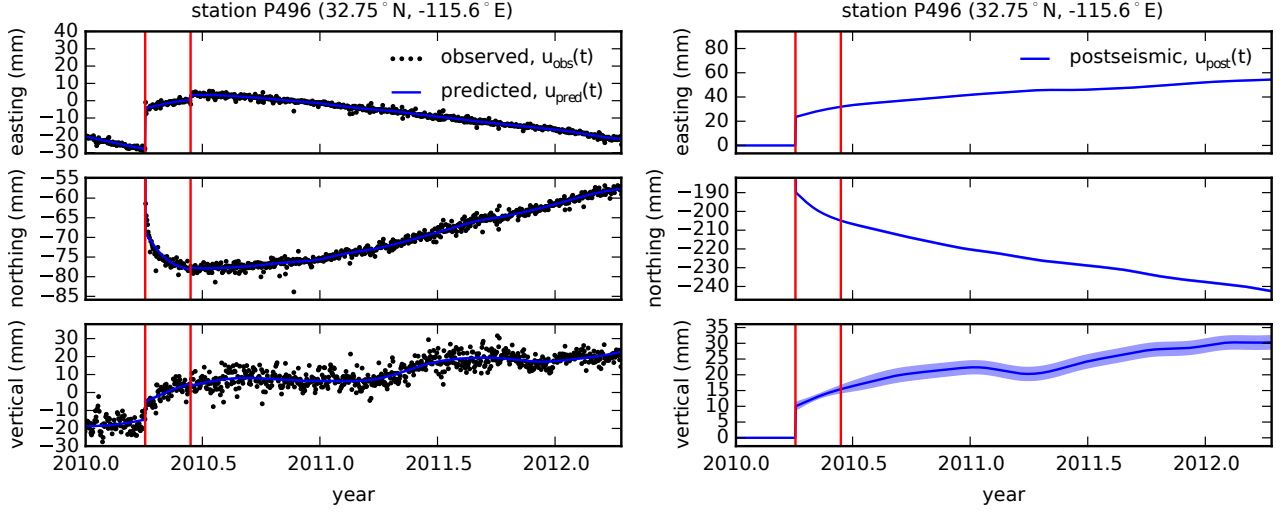
$$\Sigma_{i+1|i} = \mathbf{F}_{i+1} \Sigma_{i|i} \mathbf{F}_{i+1}^T + \mathbf{Q}_{i+1}. \quad (8)$$

This process is repeated for each of the N time epochs at which point we use Rauch-Tung-Striebel smoothing [Rauch *et al.*, 1965] to find $\mathbf{X}_{i|N}$, which is an estimate of the state at time t_i that incorporates GPS observation for all N time epochs. Our final estimates of $u_{\text{post}}(t)$ are used in subsequent analysis, while the remaining components of the state vector are considered nuisance parameters. In the interests of computational tractability, we down sample our smoothed time series from daily solutions down to weekly solutions.

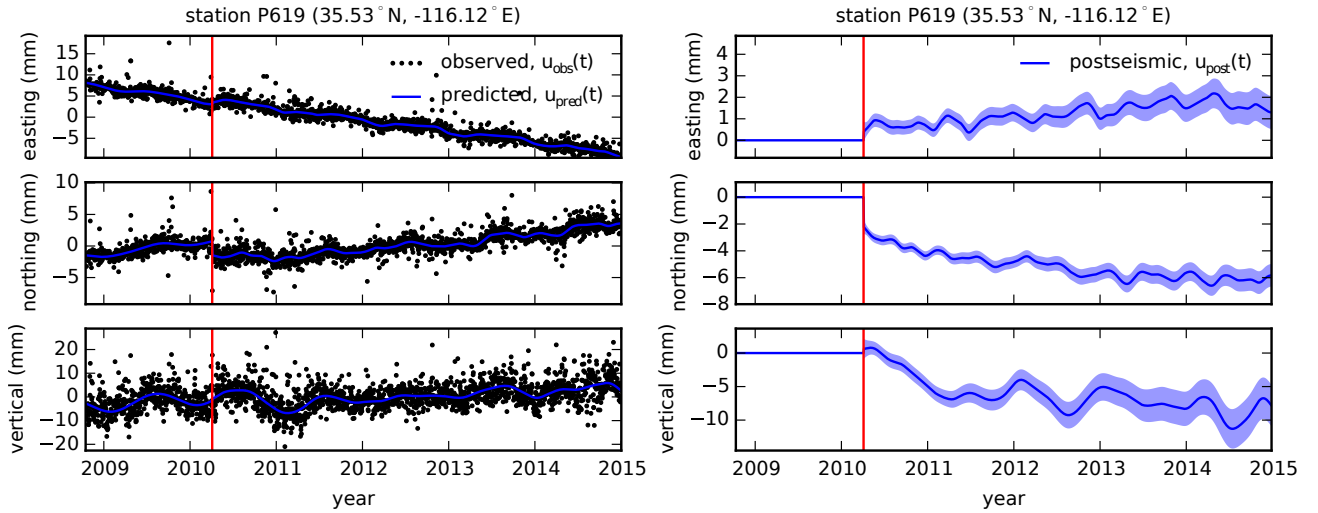
The smoothness of $u_{\text{post}}(t)$ is controlled by the chosen value of σ^2 , which describes how rapidly we expect postseismic displacements to vary over time. Setting σ^2 equal to zero will effectively result in modeling $u_{\text{post}}(t)$ as a straight line which is insufficient to describe the expected transient behavior in postseismic deformation. The other end member, where σ^2 is infinitely large, will result in $u_{\text{pred}}(t)$ over fitting the data. While one can use a maximum likelihood based approach for picking σ^2 [e.g. Segall and Mathews, 1997], we instead take a subjective approach and choose a value for σ^2 that is just large enough to faithfully describe the observed deformation at the most near-field station in our study, P496, which exhibits the most ~~pronounced~~ rapid changes in velocity. This ensures that σ^2 will be sufficiently large so that our estimate of $u_{\text{post}}(t)$ does not smooth out potentially valuable postseismic signal at the remaining stations. We find that using $\sigma^2 = 0.05 \text{ m}^2/\text{yr}^3$ adequately describe all but the first week of postseismic deformation at station P496, which ~~gets incorporated into slightly increases~~ our estimate of coseismic displacements (Figure 2). We ~~assume that the first week of deformation is overwhelmingly the result of afterslip and this afterslip is lumped into our estimates of coseismic slip. Freed *et al.* [2007] noted that postseismic deformation can be observed at distances greater than 200 km from the Hector Mine earthquake and, after filtering the time series for stations up to 400 km from include an example of estimating $u_{\text{post}}(t)$ for a far-field station, P619, which is about 359 km north of the El Mayor-Cucapah epicenter, we also clearly see far reaching postseismic transient deformation (Figure 3). At station P619, along with all the other stations in the Mojave region, there is a south-trending postseismic transience that persists for the first three years after the El Mayor-Cucapah earthquake. Postseismic deformation that extends to these epicentral distances has also been observed after the Hector Mine earthquake [Freed *et al.*, 2007].~~

It is important to note that the shown uncertainties in $u_{\text{post}}(t)$ do not account for the non-negligible epistemic uncertainty in eq. (2). For example, we assume a constant rate of secular deformation, which appears to be an appropriate approximation for all but perhaps the stations closest to the Hector Mine epicenter, as noted above. Also, our model for seasonal deformation in eq. (2) assumes a constant amplitude over time, which means that any yearly variability in the climatic conditions could introduce systematic residuals [Davis *et al.*, 2012]. Indeed, it would be more appropriate to consider the seasonal amplitudes $c_2 - c_5$ in eq. (2) as stochastic variables [Murray and Segall, 2005]. By using constant seasonal amplitudes, our estimate of $u_{\text{post}}(t)$ seems to describe some of the unmodeled annual and semi-annual oscillations (e.g. Figure 3).

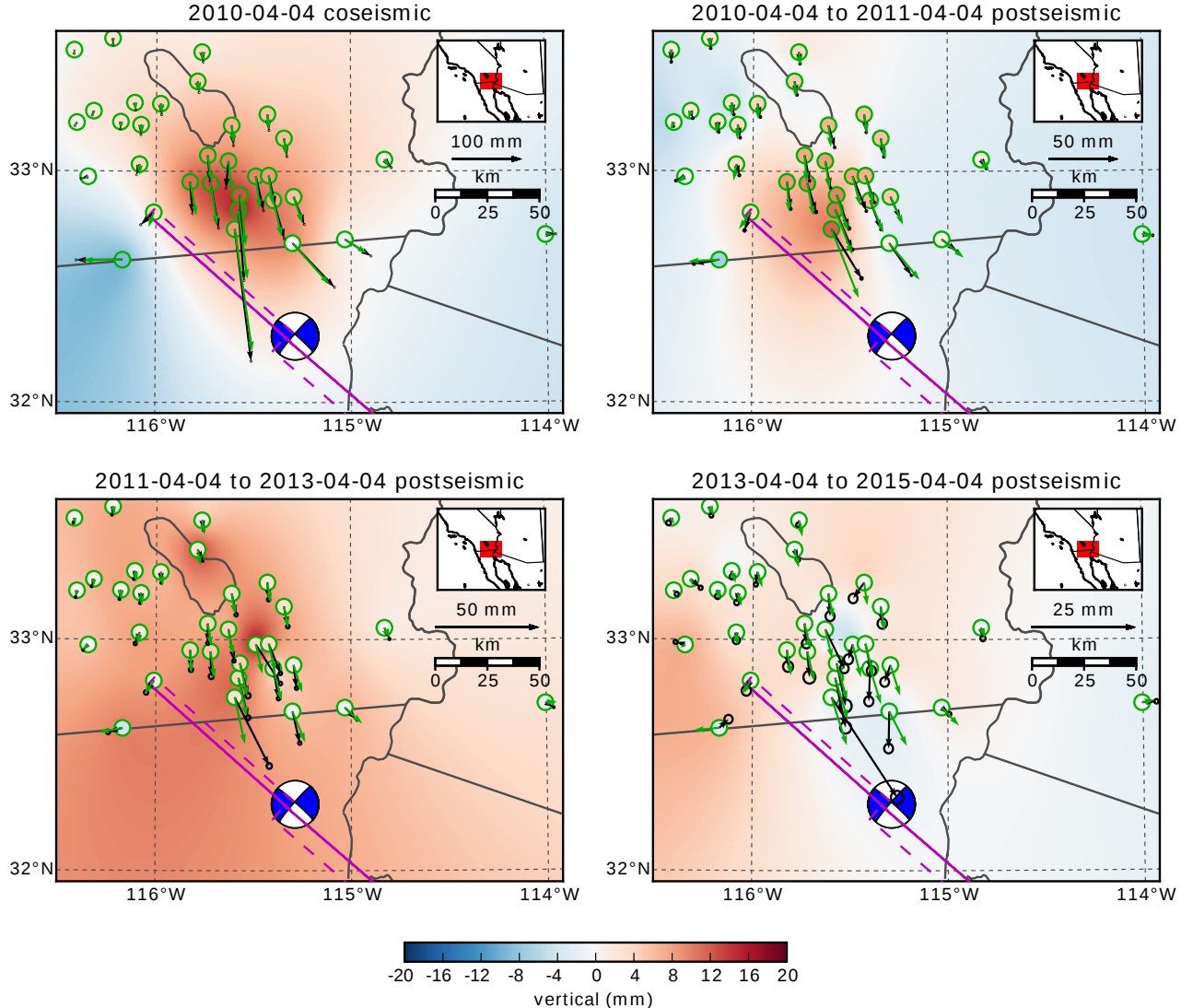
We show in Figures 4 and 5 the near and far-field postseismic displacements accumulated over the time intervals 0-1 years, 1-3 years, and 3-5 years, as well as the coseismic displacements. Stations at epicentral distances beyond ~ 200 km have an elevated rate of deformation for the first three years following the earthquake. This far-field deformation ~~has a southward trend is trending southward at a rate of a few millimeters per year~~ along the direction of the El Mayor-Cucapah P-axis and a P-axis. A similar eastward trend can be seen in the few far-field stations in Arizona, located along the T-axis-T-axis. After three years, the trend in far-field postseismic deformation is barely perceptible. Most far-field stations display an initial subsidence for the first year after the El Mayor-Cucapah earthquake followed by continued uplift. This trend in vertical deformation can be observed in all three of the quadrants where postseismic data is available, which means that the vertical deformation does not exhibit an anti-symmetric quadrant pattern, as would be expected for postseismic processes. Although we use



203 **Figure 2.** Left panels show GPS time series from UNAVCO (black)
204 and the predicted displacement (blue) from eq. (2) for a near-field station.
205 Red lines indicate the times of the El Mayor-Cucapah and Ocotillo earth-
206 quakes. The right panels show estimated coseismic and postseismic displace-
ments, u_{post} , which are extracted
from the predicted displacements. The 68% confidence interval is shown in light blue.



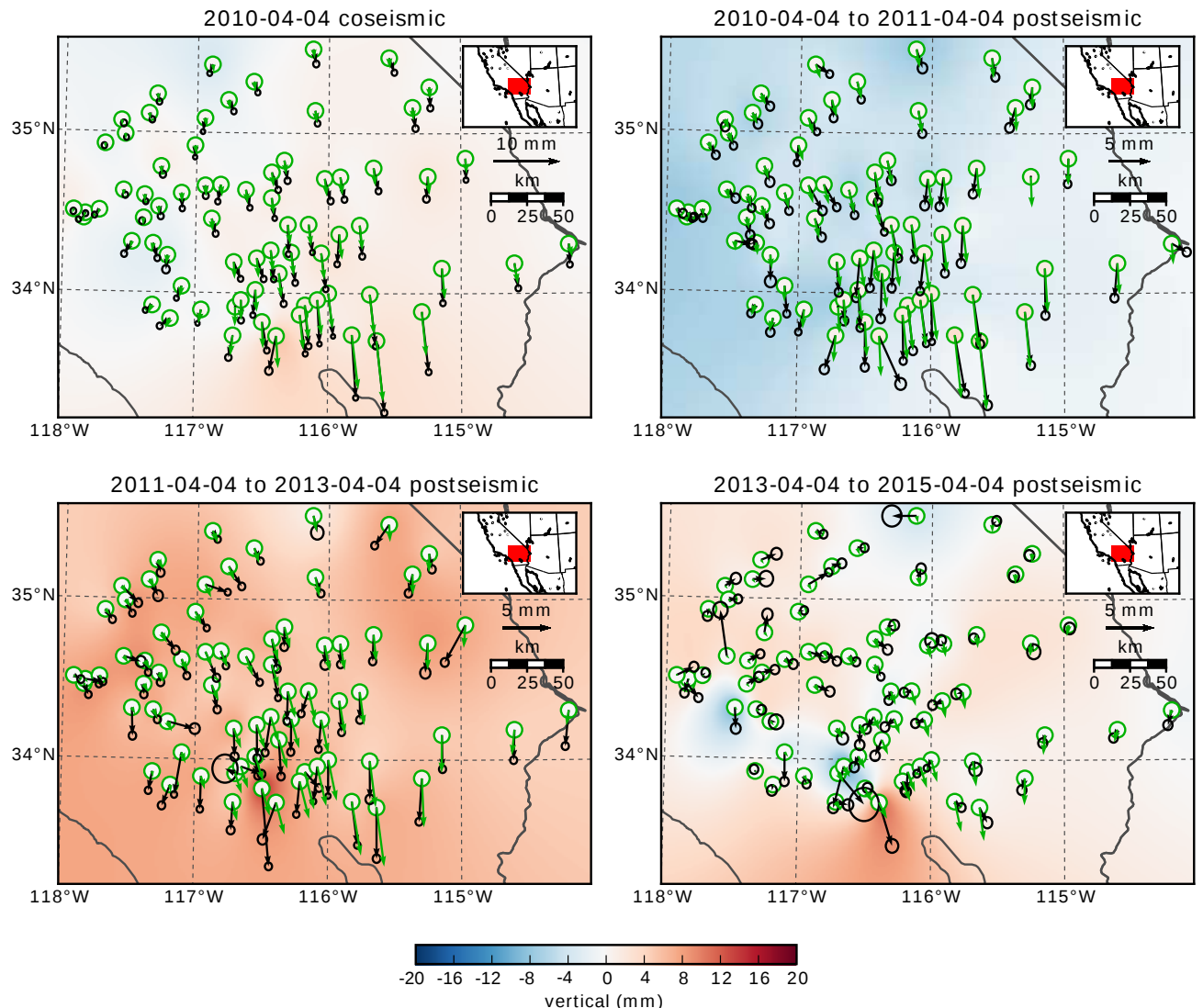
207 **Figure 3.** same as Figure 2 but for a far-field station.



232 **Figure 4.** Near-field coseismic and cumulative postseismic displacements over the indicated time periods
 233 (black) as well as and predicted displacements for our preferred model from Section 3.3 (green). Observed
 234 vertical deformation is displacements are shown as an interpolated field and predicted vertical displacements
 235 are shown within the green circles at the base of each vector. Note that the interpolant is not well constrained
 236 in Mexico where there is no data available.

230 vertical deformation in our analysis in Section 3, we do not put an emphasis on trying to de-
 231 scribe the vertical deformation as because it likely does not have postseismic origins.

238 The near-field postseismic deformation is notably sustained when compared to the far-
 239 field deformation. Namely, the station in this study which is closest to the El Mayor-Cucapah
 240 epicenter, P496, has been moving at a steady rate a steady postseismic trend of ~ 1.5 cm/yr
 241 to the south since after about one year after the **El Mayor-Cucapah earthquake**. Vertical post-
 242 seismic deformation in the near-field does display a quadrant pattern which is consistent with
 243 the coseismic vertical deformation, suggesting that it is resulting from postseismic processes.
 244 However, the vertical postseismic signal is only apparent for the first year after the earthquake
 245 (Figure 4). As with the far-field deformation, there is a general trend of uplift in the near-field
 246 after about one year.

**Figure 5.** Same as Figure 4 but for far-field stations.

depth (km)	λ (GPa)	μ (GPa)	η_{eff} (10^{18} Pa s)	μ_k/μ
0-5	24.0	24.0	-	-
5-15	35.0	35.0	-	-
15-30	42.0	42.0	44.3	0.0
30-60	61.0	61.0	5.91	0.375
60-90	61.0	61.0	1.99	0.375
90-120	61.0	61.0	1.31	0.375
120-150	61.0	61.0	1.10	0.375
150- ∞	61.0	61.0	1.07	0.375

248 **Table 1.** Assumed and estimated material properties. λ and μ are assumed known *a priori* and are based
 249 on the values used for the coseismic model by *Wei et al.* [2011b]. The values for η_{eff} are estimated in Section
 250 3.2, and $\frac{\mu_k}{\mu}$ are the optimal shear moduli ratios found in Section 3.3 for a Zener rheology upper mantle.

247 3 Postseismic Modeling

251 We seek to find the mechanisms driving five years of postseismic deformation following
 252 the El Mayor-Cucapah earthquake and we consider afterslip and viscoelastic relaxation as
 253 candidate mechanisms. Poroelastic rebound has also been used to model postseismic defor-
 254 mation [e.g. Jónsson *et al.*, 2003]; however, Gonzalez-Ortega *et al.* [2014] found that poroe-
 255 elastic rebound is unlikely to be a significant contributor to postseismic deformation following
 256 the El Mayor-Cucapah earthquake. Furthermore, we consider stations which are sufficiently
 257 far away from the main-rupture that poroelastic rebound should be insignificant.

258 We estimate coseismic and time-dependent postseismic fault slip, both of which are as-
 259 sumed to occur on a fault geometry modified from *Wei et al.* [2011b]. Field studies [*Fletcher*
 260 *et al.*, 2014] and LIDAR observations [*Oskin et al.*, 2012] have revealed a significantly more
 261 complicated fault geometry than what was inferred by *Wei et al.* [2011b], especially within the
 262 Sierra Cucapah. However, we find that a relatively simple coseismic fault geometry based on
 263 [*Wei et al.*, 2011b] is adequate because most of the stations used in this study are sufficiently
 264 far from the El Mayor-Cucapah rupture zone that they are insensitive to the details in the fault
 265 geometry found by *Fletcher et al.* [2014] and *Oskin et al.* [2012]. The fault geometry used in
 266 this study (Figure 1) consists of the two main fault segments inferred by *Wei et al.* [2011b],
 267 where the northern segment runs through the Sierra Cucapah up to the US-Mexico border and
 268 the southern segment is the Indiviso fault which extends down to the Gulf of California. Both
 269 segments extend from the surface to 15 km depth. We extend the northern segment by 40 km
 270 to the north-west, northwest, which is motivated by the clustering of aftershocks on the north-
 271 ern tip of the coseismic rupture zone [*Hauksson et al.*, 2011; *Kroll et al.*, 2013]. This extended
 272 fault segment was also found to be necessary by *Rollins et al.* [2015] and *Pollitz et al.* [2012]
 273 in order to describe the postseismic deformation.

274 3.1 Elastic Postseismic Inversion

275 We consider a variety of rheologic models for the lower crust and upper mantle. The
 276 simplest rheologic model is to consider them to be effectively elastic and isotropic. In such
 277 case, the rheologic parameters consist of the Lamé parameters, λ and μ , which are reasonably
 278 well known and we use the same values used by *Wei et al.* [2011b] throughout this paper (Ta-
 279 ble 3). The only unknown is the distribution of fault slip, which can be easily estimated from
 280 postseismic deformation through linear least squares. Using *Rollins et al.* [2015] used a sub-
 281 set of the GPS stations considered in this study, *Rollins et al.* [2015] and found that three years
 282 of postseismic deformation following the El Mayor-Cucapah earthquake can be explained with
 283 afterslip on the coseismic fault plane without requiring any viscoelastic relaxation. We also
 284 perform an elastic slip inversion, but we use GPS stations within a larger radius about the El

285 Mayor-Cucapah epicenter (400 km instead of \sim 200 km). Our forward problem describing pre-
 286 dicted postseismic deformation, u_{pred} , in terms of time dependent fault slip, s , is

$$u_{\text{pred}}(x, t) = \int_F s(\xi, t)g(x, \xi)d\xi, \quad (9)$$

287 where F denotes the fault and $g(x, \xi)$ is the elastic Green's function describing displacement
 288 at surface position x resulting from slip at ξ on the fault. We estimate coseismic slip and the
 289 rate of afterslip ~~at the discrete time intervals, over the postseismic time intervals~~ 0.0-0.125,
 290 0.125-0.25, ~~0.25-0.5~~, 0.5-1.0, 1.0-2.0, 2.0-3.0, 3.0-4.0, and 4.0-5.0 years ~~after the earthquake~~.
 291 Each fault segment is discretized into roughly 4 km by 4 km patches ~~and we estimate a strike-slip~~
 292 ~~and thrust component of slip for each patch. We an we~~ impose that the direction of slip and
 293 slip rate are within 45° of right-lateral. We also add zeroth-order Tikhonov regularization so
 294 that our solution for s satisfies

$$\min_s \left(\left\| \frac{u_{\text{pred}}(s) - u_{\text{post}}}{\sigma_{\text{post}}} \right\|_2^2 + \lambda_s \|s\|_2^2 \right), \quad (10)$$

295 where σ_{post} is the uncertainty on postseismic displacements and λ_s is a penalty parameter which
 296 is chosen with a trade-off curve. We use Pylith [Aagaard *et al.*, 2013] to compute the Green's
 297 functions for this inversion as well as for the remaining inversions in this paper.

298 Our coseismic slip and afterslip solutions are shown in Figure 6. ~~As with Similar to Rollins~~
 299 *et al.* [2015], we find that a large amount of afterslip on the ~~southern Indiviso~~ fault segment
 300 is required to explain the observations. The potency of our inferred coseismic slip is $3.2 \times$
 301 10^9 m^3 , equivalent to a ~~Mw7.28~~ $\text{Mw}=7.28$ earthquake when assuming a shear modulus of 32
 302 GPa. The potency of our inferred cumulative five years of afterslip is $6.1 \times 10^9 \text{ m}^3$, equiv-
 303 alent to a ~~Mw7.46~~ $\text{Mw}=7.46$ earthquake, which is unrealistically large if we consider after-
 304 slip to be driven by coseismically induced stresses. Figure ??-7 shows the time series for the
 305 observed and predicted postseismic displacements at stations along the El Mayor-Cucapah ~~P~~
 306 ~~axis~~ P-axis . We show the radial component of displacements with respect to the El Mayor-Cucapah
 307 epicenter and we also rescale the displacements so that the difference between the minimum
 308 and maximum observed displacements are the same for each station. Our elastic slip model
 309 accurately describes near-field postseismic deformation and systematically underestimates post-
 310 seismic deformation at epicentral distances $\gtrsim 150$ km. When the fault segments used in the
 311 inversion are extended down to 30 km depth, rather than 15 km, the systematic far-field resid-
 312 uals are smaller but remain apparent. Because an elastic model requires an unrealistic amount
 313 of afterslip and is unable to predict far-field deformation, we move on to consider viscoelas-
 314 tic models in the next section.

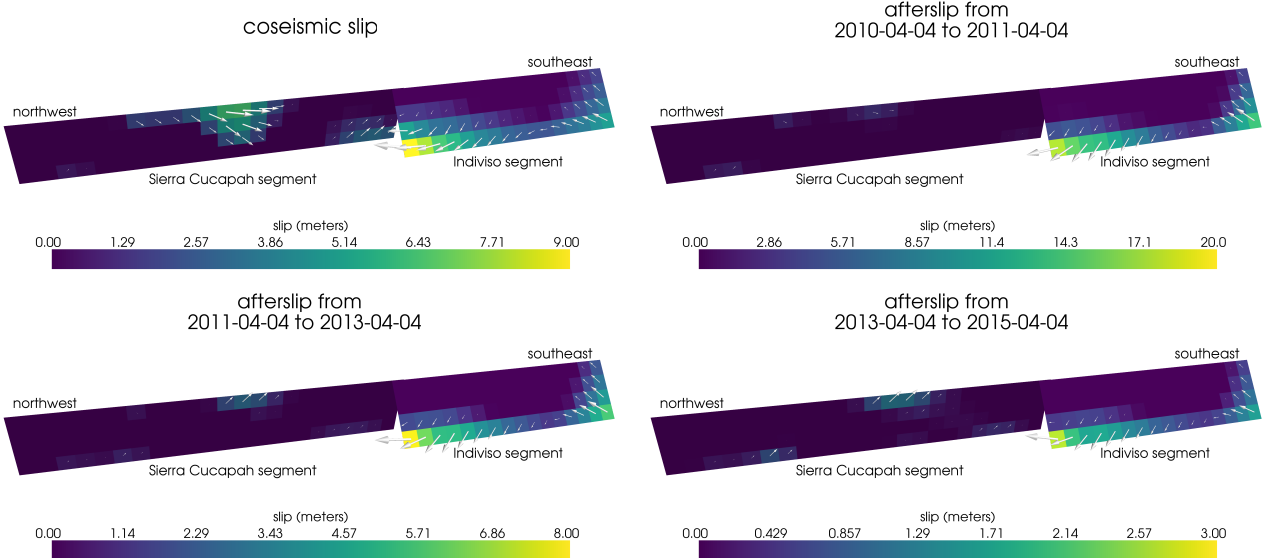
328 3.2 Early Postseismic Inversion

329 For any linear viscoelastic rheology of the crust and mantle, postseismic displacements
 330 resulting from time dependent fault slip can be described as

$$u_{\text{pred}}(x, t) = \int_F s(\xi, t)g(x, \xi)d\xi + \int_0^t \int_F s(\xi, \tau)f(t - \tau, x, \xi)d\xi d\tau, \quad (11)$$

331 where $f(t, x, \xi)$ describes the time-dependent velocity at x resulting from viscoelastic relax-
 332 ation of stresses induced by slip at ξ . f is a function of λ , μ , and any additional rheologic pa-
 333 rameters controlling the viscoelastic response, which are generally not well known. Schematic
 334 representations of the viscoelastic rheologic models considered in this study are shown in Fig-
 335 ure 8. We discuss these rheologic models and their use in geophysical studies in Section 4.

338 In order to greatly simplify the inverse problem, we use the method described in *Hines*
 339 and *Hetland* [2016] to constrain an initial effective viscosity structure from the early postseis-
 340 mic deformation. Our method ~~utilizes~~ uses the fact that coseismic stresses throughout the crust



315 **Figure 6.** Coseismic slip and cumulative afterslip over the indicated time intervals for when assuming
 316 the crust and mantle are elastic model from Section 3.1. Color indicates the magnitude of slip while arrows
 317 indicate the motion of the hanging wall.

341 and upper mantle depend on the instantaneous elastic parameters and are independent of the
 342 viscoelastic parameters which we wish to estimate. Immediately following an earthquake, each
 343 parcel will have a strain rate that is proportional to the coseismic stress and inversely propor-
 344 tional to the parcel's effective viscosity, η_{eff} . Using one-dimensional viscoelastic rheologic mod-
 345 els, we define the effective viscosity as

$$\eta_{\text{eff}} = \frac{\sigma}{\dot{\varepsilon}} \Big|_{t=0}, \quad (12)$$

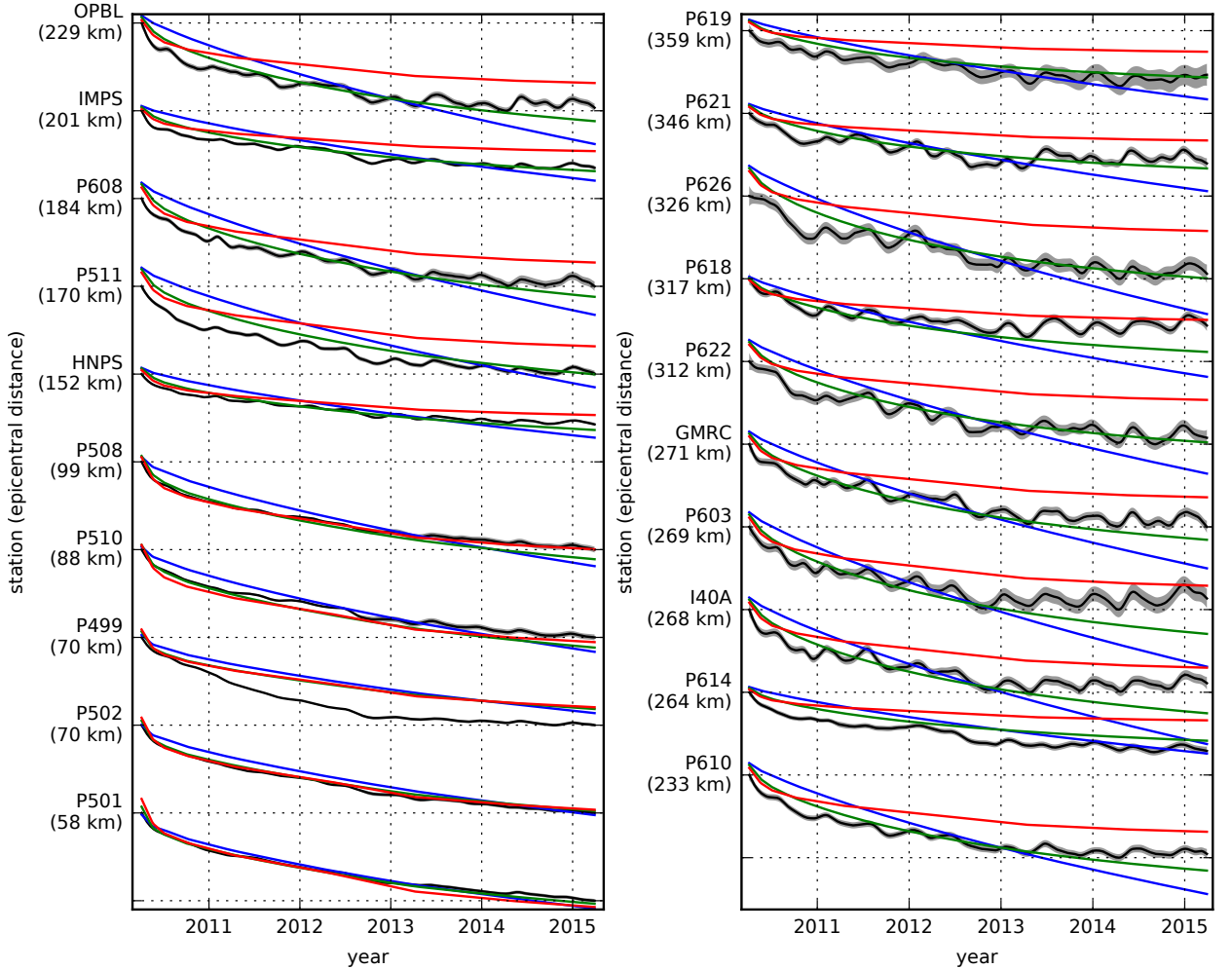
346 where σ is an applied stress at $t = 0$ and $\dot{\varepsilon}$ is the resulting strain rate. Figure 8 shows how
 347 η_{eff} relates to the parameters for various linear viscoelastic rheologies. We can deduce that the
 348 initial rate of surface deformation resulting from viscoelastic relaxation is a summation of the
 349 surface deformation resulting from relaxation in each parcel, scaled by the reciprocal of the
 350 parcel's effective viscosity. That is to say

$$f(0, x, \xi) = \int_L \frac{h(x, \xi, \zeta)}{\eta_{\text{eff}}(\zeta)} d\zeta, \quad (13)$$

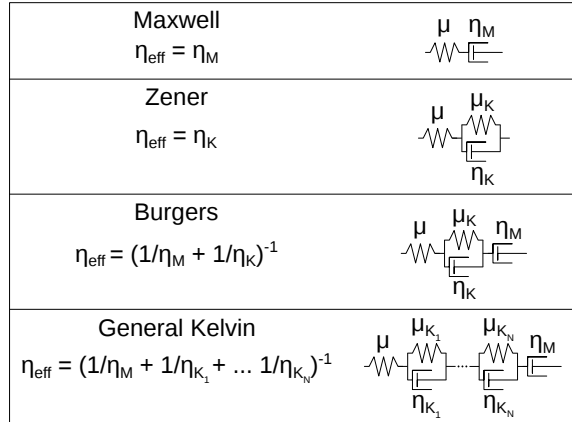
351 where L denotes the crust and mantle and $h(x, \xi, \zeta)$ describes the initial rate of deformation
 352 resulting from viscoelastic relaxation at ζ induced by slip at ξ . We can combine eq. (13) with
 353 eq. (11) to get a first-order-first-order approximation for early postseismic deformation,

$$u_{\text{pred}}(x, t) \approx \int_F s(\xi, t) g(x, \xi) d\xi + \int_0^t \int_F \int_L \frac{s(\tau, \xi)}{\eta_{\text{eff}}(\zeta)} h(x, \xi, \zeta) d\zeta d\xi d\tau, \quad (14)$$

354 which is valid for as long as the rate of deformation resulting from viscoelastic relaxation is
 355 approximately constant. Although eq. (14) may only be valid for a short portion of the post-
 356 seismic period, its utility becomes apparent when noting that g and h are only functions of
 357 the fault geometry and instantaneous elastic properties, λ and μ , and thus g and h can be com-
 358 puted numerically as a preprocessing step. The forward problem in eq. (14) can then be rapidly
 359 evaluated for any realization of s and η_{eff} . This is in contrast to evaluating the full forward



318 **Figure 7.** Scaled radial component of observed postseismic displacements u_{obs} (black) and displacements
 319 predicted by the best fitting elastic model u_{pred} (blue). Downward motion indicates that the station is
 320 moving toward the El Mayor-Cucapah epicenter. Displacement time series are scaled so that the minimum and
 321 maximum observed values lie on the grid lines. The observed postseismic displacements, u_{post} are shown
 322 in black with gray indicating the 68% confidence interval. The displacements predicted by the best fitting
 323 elastic model are shown in red. The blue and green lines are the predicted postseismic displacements for the
 324 observed models discussed in Section 3.3. The blue lines show the predicted displacements for the model
 325 with a Maxwell viscoelastic lower crust and upper mantle. The green line shows the predicted displacements
 326 for the model with a Maxwell viscoelastic lower crust and a Zener viscoelastic upper mantle. The effective
 327 viscosities are the same for both models and are shown in gray Figure 12.



336 **Figure 8.** Schematic illustration of the rheologic models considered in this paper as well as their effective
 337 viscosities.

360 problem, eq. (11), numerically for each realization of s and the unknown rheologic properties.
 361

362 Details on how eq. (14) is used to estimate s and η_{eff} from postseismic deformation can
 363 be found in *Hines and Hetland* [2016]. A non-linear Kalman filter based inverse method can
 364 also be used to estimate s and η_{eff} in a manner ~~akin~~-similar to *Segall and Mathews* [1997] or
 365 *McGuire and Segall* [2003], in which we would not have to explicitly impose a time depen-
 366 dent parametrization of s . We have thoroughly explored Kalman filter based approaches, but
 367 we ultimately prefer the method described in *Hines and Hetland* [2016] because of its rela-
 368 tive simplicity. Moreover, we believe the piecewise continuous representation of slip with re-
 369 spect to time ~~to-be-is~~ sufficiently general for the resolving power of these GPS data.

370 We estimate coseismic slip and afterslip with the same spatial and temporal discretiza-
 371 tion as in Section 3.1. Simultaneously, we estimate η_{eff} within six vertically stratified layers
 372 which have depths ranging from 15-30 km, 30-60 km, 60-90 km, 90-120 km, 120-150 km,
 373 ~~as well as and~~ from 150 km to the bottom of our numerical model domain at 800 km. We again
 374 restrict fault slip to occur between 0 and 15 km depth, which is done in order to help elim-
 375 inate inevitable non-uniqueness in the inversion. It ~~has long been recognized is well understood~~
 376 that fault slip at sufficiently great depths can produce surface deformation that is indistin-
 377 guishable from viscoelastic relaxation, at least in two-dimensional earthquake models [*Savage*, 1990].
 378 Additionally, we note that when simultaneously estimating both afterslip and viscosity in the
 379 lower crust, the inverse problem becomes particularly ill-posed. This ill-posedness is illustrated
 380 in Figure 9, which shows the displacements resulting from a meter of slip on a fault extend-
 381 ing from 15 to 30 km depth and the initial velocity resulting from subsequent viscoelastic re-
 382 laxation in the lower crust, which is given a viscosity of 10^{18} Pa s. In this demonstration, the hori-
 383 zontal dis-
 384 placements from fault slip are in the opposite direction as the displacements resulting from
 385 viscoelastic relaxation. This means that surface displacements resulting from afterslip at lower
 386 crustal depths can be cancelled out, at least partially, by a low viscosity lower crust. We eli-
 387 minate this null space by allowing only one mechanism in the lower crust, which we choose to
 388 be viscoelastic relaxation. This is not to say that we do not believe deep afterslip to be a pos-
 389 sibility; rather, we restrict slip to seismogenic depths as a modeling necessity. Although, it has
 390 been noted that the pattern of vertical postseismic deformation following the El Mayor-Cucphah
 391 earthquake indicates that a significant amount of afterslip must be shallow [*Rollins et al.*, 2015].

398 We must determine at which point the early postseismic approximation breaks down, which
 399 we will denote as t_{bd} . As noted, eq. (14) is valid for ~~approximately~~-as long as the rate of de-

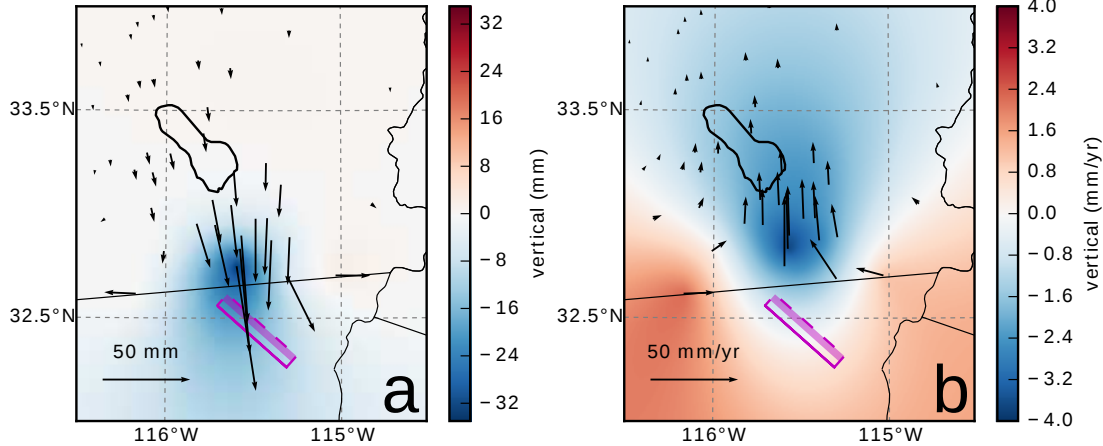


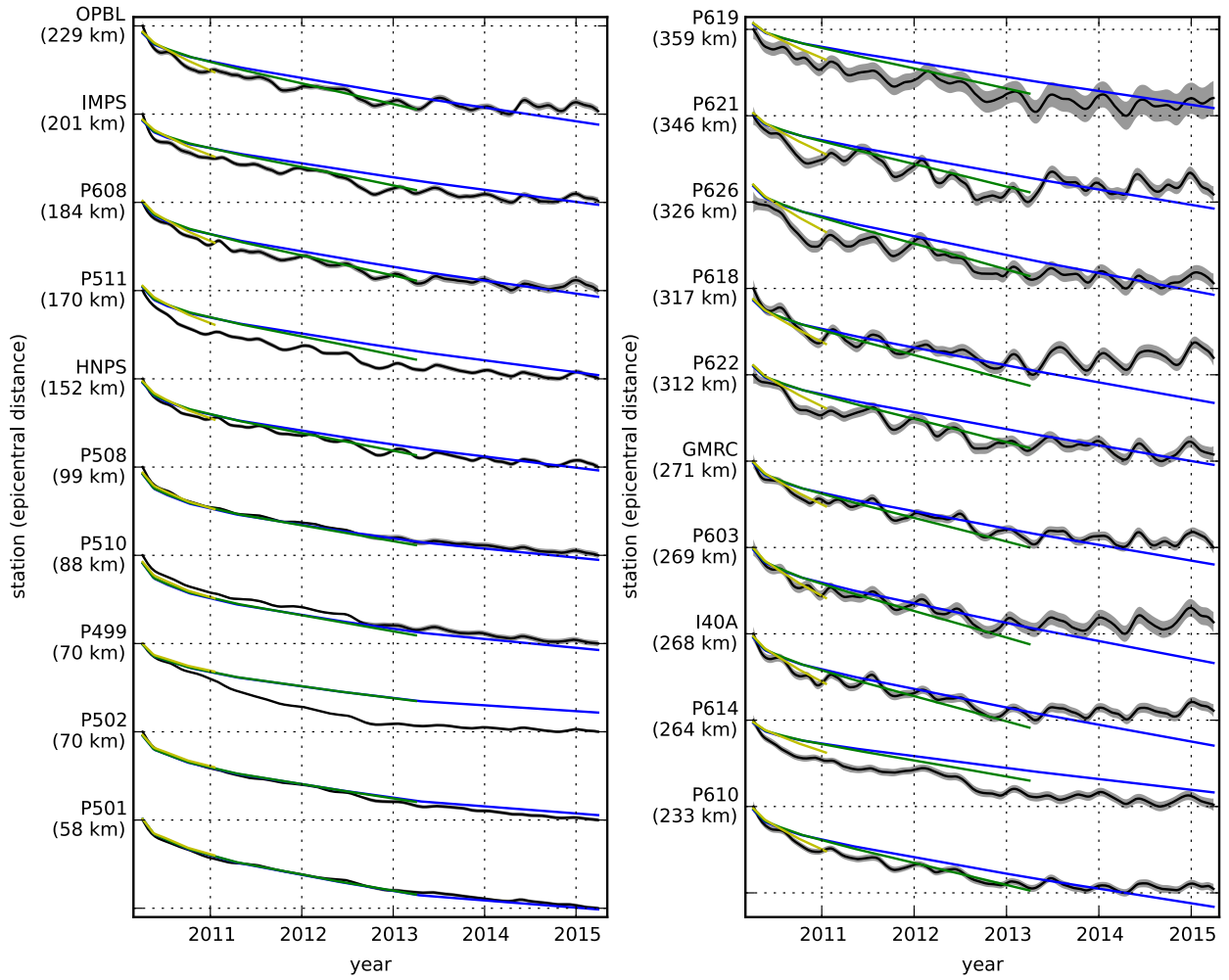
Figure 9. Displacements resulting from fault slip at lower crustal depths (a), and initial velocities resulting from subsequent relaxation of a viscoelastic lower crust (b). The fault segment dips 75° to the north-east and its surface projection is outlined in magenta. The highlighted area on the fault extends from 15 to 30 km depth and indicates where 1 meter of right-lateral slip was imposed. The elastic properties of the crust and mantle are the same as in Table 31, and η_{eff} is 10^{18} Pa s in the lower crust. Vertical displacements are interpolated between station locations.

formation resulting from viscoelastic relaxation is approximately constant. We can almost certainly assume that deformation at the most far-field stations, which are ~ 400 km away from the El Mayor-Cucapah epicenter, is the result of viscoelastic relaxation. The approximation should then be valid for as long as a linear trend adequately approximates the far-field deformation. Using this logic, it would appear that t_{bd} is about one year after the El Mayor-Cucapah earthquake. Another way to determine t_{bd} is to find the best fitting prediction of eq. (14) to observed deformation using increasing durations of the postseismic time series. t_{bd} should be the point when eq. (14) is no longer capable of describing the observed deformation without incurring systematic misfits. When using eq. (14) to fit the entire five years of postseismic displacements, we see that the near-field displacements (e.g., station P501) are accurately predicted. When looking at displacements in the far-field (e.g., station P621), we see that eq. (14) overestimates the rate of deformation in the later postseismic period and underestimates the rate of deformation in the early period (Figure 10). Due to the low signal-to-noise ratios for far-field stations, it is difficult to determine at what point eq. (14) is no longer able to predict the observed displacements; however, we settle on $t_{\text{bd}} = 0.8$ years after the earthquake, while acknowledging that the choice is subjective. As noted in Hines and Hetland [2016], overestimating t_{bd} will result in a bias towards overestimating η_{eff} , while picking a t_{bd} which is too low will not necessarily result in a biased estimate of η_{eff} , although the uncertainties would be larger. We can then consider inferences of η_{eff} to be an upper bound on the viscosity needed to describe the far-field rate of deformation during the first 0.8 years of postseismic deformation.

We estimate coseismic slip, afterslip, and effective viscosities by solving

$$\min_{s, \eta_{\text{eff}}} \left(\left\| \frac{u_{\text{pred}}(s, \eta_{\text{eff}}) - u_{\text{post}}}{\sigma_{\text{post}}} \right\|_2^2 + \lambda_s \|s\|_2^2 + \lambda_\eta \|\nabla \eta_{\text{eff}}^{-1}\|_2^2 \right), \quad (15)$$

where u_{post} consists of the first 0.8 years of postseismic deformation and u_{pred} are the predicted displacements from eq. (14). Due to inherent non-uniqueness, we have added zeroth-order Tikhonov regularization to estimates of s and second-order Tikhonov regularization to estimates of effective fluidity η_{eff}^{-1} . The degree to which we impose the regularization on slip



421 **Figure 10.** Observed postseismic displacements (black) and best fitting predictions of eq. (14) to 5.0 (blue),
 422 3.0 (green), and 0.8 (yellow) years of the postseismic data.

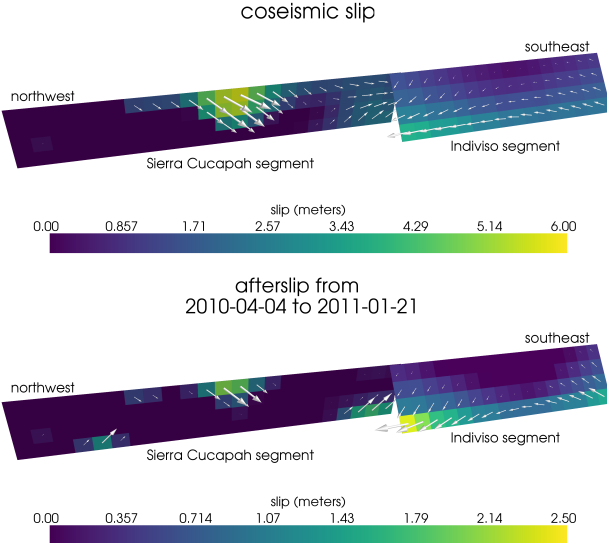
428 and fluidity is controlled by the penalty parameters λ_s and λ_η , which are chosen with trade-
 429 off curves ([Figure S1](#)). Our goal [here](#) is to get a prior constraint on η_{eff} to minimize the amount
 430 of searching we have to do when describing the postseismic deformation over the full five years,
 431 which we do in Section 3.3. Estimates of s made here will not be used in Section 3.3, and
 432 so the motivation behind adding regularization to s is to ensure that the slip driving viscoelas-
 433 tic relaxation in eq. (14) is sensible.

434 Our [estimated effective viscosities, and corresponding fluidities, are shown in Figure 12](#).
 435 [Although fluidity is rarely used in geophysical literature, eq. \(13\) is linear with respect to fluidity](#)
 436 [and so the fluidity indicates the amplitude of the viscoelastic signal coming from each layer](#).
 437 [We also show the 95confidence intervals for estimated viscosities and fluidities but we note](#)
 438 [that the uncertainties tend to be underestimated due to the added regularization \[Aster et al., 2011\]](#).
 439 [A robust feature that we see is that the largest jump in fluidity is at 60 km depth, which is consistent](#)
 440 [with the range of lithosphere–asthenosphere boundary depths inferred by Lekic et al. \[2011\]](#).
 441 [This transitional depth is also consistent with the the viscosity structure required to explain](#)
 442 [far-field postseismic deformation following the Hector Mine earthquake \[Freed et al., 2007\]](#).
 443 [We find that the viscosity below 60 km depth needs to be \$\sim 10^{18}\$ Pa s to describe the early](#)
 444 [rate of postseismic deformation at far-field stations while the lower crust and uppermost mantle](#)
 445 [need to be relatively stronger. The viscosity of the lower crust is the least well constrained as](#)
 446 [there is no evidence of relaxation in that layer, meaning that it is effectively elastic over the](#)
 447 [first 0.8 years after the earthquake](#).

448 [Effective viscosities and associated fluidities inferred by fitting eq. \(14\) to the first 0.8](#)
 449 [years of postseismic displacements. 95confidence intervals, estimated from bootstrapping, are](#)
 450 [indicated by color fields](#).

451 Our initial estimate for coseismic slip and cumulative afterslip over the first 0.8 years
 452 after the El Mayor-Cucapah earthquake are shown in Figure 11. Similar to our elastic slip model
 453 from Section 3.1, a significant amount of right-lateral and normal coseismic slip is inferred
 454 to be on the Sierra Cucapah [fault](#) segment. Our coseismic slip solution [on the Sierra Cucapah](#)
 455 [segment](#) is consistent with field studies [Fletcher et al., 2014] and the model from Wei et al.
 456 [2011b]. [Our inferred slip on the Indiviso fault segment differs from Wei et al. \[2011b\] because](#)
 457 [the GPS data used in this study is not capable of resolving the spatial distribution of fault slip](#)
 458 [on that segment \(Figure S2\)](#). The potency of inferred coseismic slip is 3.3×10^9 m³, which
 459 is also about the same as that inferred from Section 3.1. The present inference of afterslip on
 460 the Indiviso fault is significantly less than what was found in the Section 3.1 where we did
 461 not account for viscoelasticity. When fault slip is simultaneously estimated with viscosity, the
 462 potency of inferred afterslip over the first 0.8 years after the earthquake is 0.85×10^9 m³, com-
 463 pared to 3.5×10^9 m³ when we assume the crust and upper mantle are elastic. The signifi-
 464 cant amount of afterslip inferred on the Indiviso fault [in Section 3.1](#) seems to be compensat-
 465 ing for unmodeled viscoelastic relaxation[at depths greater than 60 km](#). The fact that there is
 466 still an appreciable amount of afterslip inferred on the Indiviso fault raises the question of whether
 467 it is compensating for viscoelastic relaxation that is more localized than what we allow for since
 468 we only estimate depth dependent variations in viscosity.

469 Our [estimated effective viscosities, and corresponding fluidities, are shown in Figure 12](#).
 470 [Although fluidity is rarely used in geophysical literature, eq. \(13\) is linear with respect to fluidity](#)
 471 [and so the fluidity indicates the amplitude of the viscoelastic signal coming from each layer](#).
 472 [We use bootstrapping to find the 95% confidence intervals for our estimated effective viscosities](#)
 473 [which are shown as shaded regions in Figure 12. It is important to remember that the presented](#)
 474 [effective viscosities were estimated with a smoothing regularization constraint and so the uncertainties](#)
 475 [are almost certainly underestimated \[Aster et al., 2011\]](#). Indeed, many viscosity profiles which
 476 [are outside of the shown confidence intervals can just as adequately described the first 0.8 years](#)
 477 [of postseismic deformation. Our solution in Figure 12 should be interpreted as the smoothest](#)
 478 [effective viscosity profile which is capable of describing the data. This means that any sharp](#)
 479 [viscosity transitions will be tapered out in the inversion, which we demonstrate with a synthetic](#)
 480 [test in Figure S2. Nonetheless, a robust feature that we see is that the largest jump in fluidity](#)



489 **Figure 11.** Coseismic slip and afterslip inferred by fitting eq. (14) to the first 0.8 years of postseismic
490 displacements.

481 is at 60 km depth, which is consistent with the range of lithosphere-asthenosphere boundary
482 depths inferred by Lekic *et al.* [2011]. This transitional depth is also consistent with the the
483 viscosity structure required to explain far-field postseismic deformation following the Hector
484 Mine earthquake [Freed *et al.*, 2007]. We find that the viscosity below 60 km depth needs to
485 be $\sim 1 \times 10^{18}$ Pa s to describe the early rate of postseismic deformation at far-field stations
486 while the lower crust and uppermost mantle need to be relatively stronger. The viscosity of
487 the lower crust has the largest uncertainties because there is no evidence of relaxation in that
488 layer, meaning that it is effectively elastic over the first 0.8 years after the earthquake.

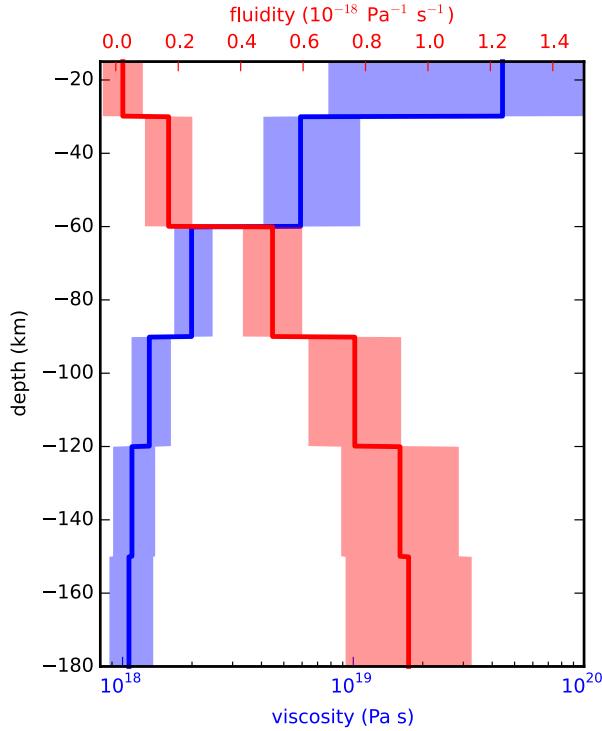
494 3.3 Full Postseismic Inversion

495 In the previous section, we used the inverse method from Hines and Hetland [2016] to
496 constrain the effective viscosity structure required to explain the first 0.8 years of postseismic
497 deformation. In this section, we use these effective viscosities as a prior constraint when search-
498 ing for models which are capable of describing the available five years of postseismic data,
499 where our forward problem is now eq. (11) rather than the approximation given by eq. (14).
500 We perform a series of fault slip inversions assuming a variety of rheologies for the lower crust
501 and upper mantle which are consistent with our findings from Section 3.2. We appraise each
502 model using the mean chi-squared value,

$$\chi^2 = \frac{1}{N} \left\| \frac{\mathbf{u}_{\text{pred}} - \mathbf{u}_{\text{obs}}}{\sigma_{\text{obs}}} \frac{\mathbf{u}_{\text{pred}} - \mathbf{u}_{\text{post}}}{\sigma_{\text{post}}} \right\|_2^2, \quad (16)$$

503 where N is the number of observations.

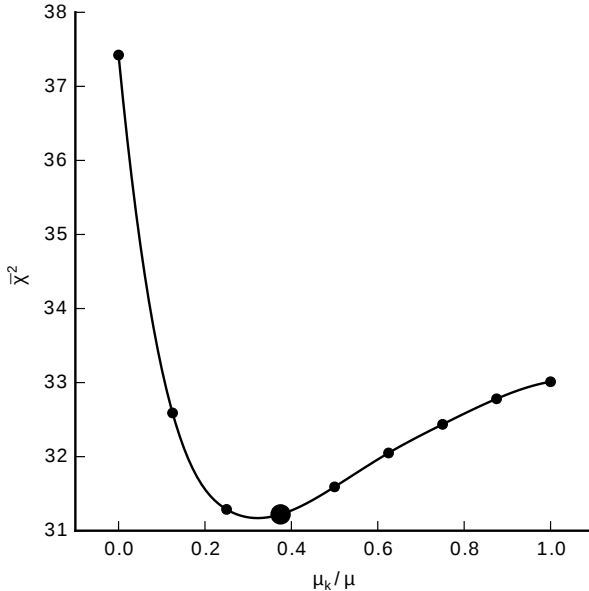
504 We first assume that the crust and mantle can be described with a Maxwell rheology,
505 and we set the steady-state viscosity η_M equal to our inference of η_{eff} . We compute f and
506 g from eq. (11) using Pylith, and we use the same spatial and temporal discretization of s as
507 in Sections 3.1 and 3.2. We estimate s using linear least squares and find a misfit of $\bar{\chi}^2 =$
508 37.4. For comparison, $\bar{\chi}^2 = 35.3$ for the elastic model from Section 3.1. The Maxwell vis-



491 **Figure 12.** Effective viscosities and associated fluidities inferred by fitting eq. (14) to the first 0.8 years of
 492 postseismic displacements. 95% confidence intervals, estimated from bootstrapping, are indicated by shaded
 493 regions.

509 coelastic model has a larger misfit because it tends to overestimate the rate of deformation af-
 510 ter about three years (Figure ??). Since our initial estimates of η_{eff} may be biased towards
 511 overestimating viscosities, we have also performed the slip inversion where we use uniformly
 512 lower viscosities in the crust and mantle. However, however, decreasing the viscosity only in-
 513 creases the misfit. Although, the viscosities used here are consistent with the successful Maxwell
 514 viscoelastic models found by *Rollins et al.* [2015] and *Spinler et al.* [2015], which had man-
 515 tle viscosities on the order of 10^{18} Pa s and relatively higher lower crustal viscosities, we find
 516 that such a model is incapable of describing the entire postseismic time series. *Pollitz et al.*
 517 [2001] similarly recognized this deficiency in a Maxwell rheology, which then motivated their
 518 exploration of a Burgers rheology upper mantle [*Pollitz*, 2003].

519 Instead of exploring a Burgers rheology mantle, which introduces two new parameters
 520 that need to be estimated, the transient viscosity η_K and transient shear modulus μ_K , we first
 521 consider a Zener rheology for the mantle, which only introduces one additional unknown pa-
 522 rameter, μ_K . We assume that the lower crust still has a Maxwell rheology. The steady-state
 523 viscosity in the crust and the transient viscosity in the mantle are set equal to the inferred ef-
 524 fective viscosities. We then estimate the ratio of shear moduli $\frac{\mu_K}{\mu}$. We compute nine differ-
 525 ent sets of Green's functions, f and g , where we assume values of $\frac{\mu_K}{\mu}$ ranging from 0 to 1.
 526 The former being a degenerate case where the Zener model reduces to the above Maxwell model.
 527 We estimate coseismic slip and afterslip for each realization of $\frac{\mu_K}{\mu}$. The We find that a shear
 528 moduli ratio that of 0.375 yields the best prediction to the observed postseismic displacements
 529 is found to be 0.375 which produces with a misfit of $\chi^2 = 31.2$ (Figure 13). The improve-
 530 ment in the Zener model over the Maxwell model can be clearly seen in the fit to the far-field
 531 data (Figure ??). The 7) where the Zener model does a significantly better job at explaining



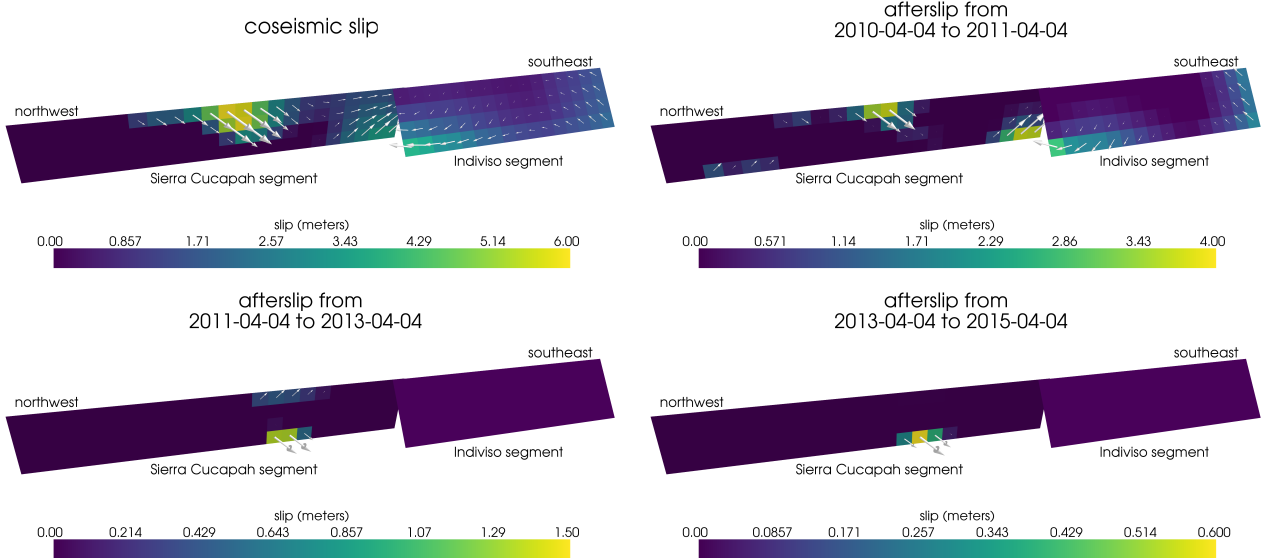
534 **Figure 13.** Mean chi-squared value for the best fitting slip model as a function of the transient shear modu-
 535 lus relative to the elastic shear modulus in a Zener upper mantle. Large dot indicates our preferred ratio.

532 the transient rate of ~~far-field~~-deformation throughout the five years ~~considered in this study~~.
 533 ~~The rheologic parameters for our preferred Zener model are summarized in Table 1.~~

536 ~~Observed postseismic displacements (black). Predicted postseismic displacements for the
 537 best fitting slip model when assuming a Maxwell viscoelastic lower crust and upper mantle
 538 (blue). Predicted postseismic displacements for the best fitting slip model when assuming a
 539 Maxwell viscoelastic lower crust and a Zener viscoelastic upper mantle (green). The effective
 540 viscosities are the same for both models and are shown in Figure 12.~~

541 Because we are able to adequately describe the available five years of postseismic de-
 542 formation with a Zener model, we do not find it necessary to explore the parameter space for
 543 a more complicated Burgers rheology. However, since the Zener model is a Burgers model with
 544 an infinite steady-state viscosity, we can conclude that any Burgers rheology that has a tran-
 545 sient viscosity consistent with that found in Section 3.2 and a steady-state viscosity $\gtrsim 10^{20}$
 546 Pa s, which is effectively infinite on the time scale of five years, would also be able to sat-
 547 isfactorily describe the observable postseismic deformation.

548 The regularized inference of coseismic slip and afterslip for our preferred Zener model
 549 is shown in Figure 14. The inferred coseismic potency is 3.0×10^9 m³, equivalent to a ~~Mw7.26~~
 550 ~~earthquake, and Mw=7.26 earthquake, where~~ most of the slip is shallow and on the Sierra Cu-
 551 capah fault segment. The potency of five years of afterslip is 1.1×10^9 m³. Most of the af-
 552 terslip in our preferred model occurs within the first year after the earthquake and coincides
 553 with the location of our inferred coseismic slip. Inferred afterslip within the first year is ac-
 554 counting for the most rapid near-field transient deformation. After one year, afterslip is inferred
 555 to be deeper down on the Sierra Cucapah segment, which is describing much of the sustained
 556 near-field postseismic deformation. We emphasize, that the GPS station closest to where we
 557 infer afterslip, P496, is still about 30 km away, which is too far for us to conclusively argue
 558 for sustained localized deformation rather than shallow distributed deformation. The deep af-
 559 terslip inferred after one year could potentially be describing deformation resulting from lower
 560 crustal flow. To test this, we have modified our preferred model by decreasing the lower crustal
 561 viscosity from 5.91×10^{19} Pa s to 1×10^{19} Pa s, which is still consistent with our viscosity
 562 inference from Section 3.2, and ~~we~~ inverted for fault slip. We find that a model with a weaker



590 **Figure 14.** Inferred coseismic slip and afterslip when assuming a Maxwell rheology in the lower crust and
 591 a Zener rheology in the upper mantle. The transient viscosity η_K in the mantle and steady-state viscosity η_M
 592 in the crust are set equal to the effective viscosities from Figure 12. We set $\frac{\mu_K}{\mu} = 0.375$ in the upper mantle.

563 lower crust adequately describes the postseismic displacements without any afterslip after one
 564 year, while still requiring about the same amount of afterslip over the first year. We do believe
 565 that the early, shallow afterslip on the Sierra Cucapah segment is a robust feature in our pre-
 566 ferred model, while we are not confident in our inference of later deep afterslip.

567 ~~the~~ The postseismic displacements predicted by our preferred Zener model are shown
 568 in Figures 4, 5 and ???. Overall, the trends in the near-field and far-field transient deformation
 569 are accurately described. In particular, the trends in far-field deformation are much better described
 570 by our preferred Zener model than either an elastic model or a model with a Maxwell viscoelastic
 571 mantle (Figure ??). There are a few areas where we have notable misfit. Most of our misfit
 572 is for the near-field stations in 7. The largest misfit occur within the Imperial Valley, and we
 573 attribute this misfit to our relatively simple fault geometry, which does not account for potential
 574 and there does not appear to be any systematic trend in the residuals. This suggests that the
 575 large errors are due to localized processes such as fault slip in the Imperial Valley triggered
 576 by the El Mayor-Cucapah earthquake [Wei et al., 2011a, 2015]. In particular, we are unable
 577 to model the sustained, rapid rate of deformation at station P496, which suggests that this station
 578 could be influenced by a more localized deformation mechanism than is considered in this study. We
 579 do not see any pattern in the residuals that would suggest a laterally heterogeneous viscosity
 580 structure, which has been explored by Pollitz et al. [2012] and Rollins et al. [2015]. We do
 581 notice regionally uniform seasonal oscillations in the lateral and vertical components of the
 582 residuals with an amplitude of 1-2 millimeters. This is the result of our method for data processing
 583 which is not able to completely remove the seasonal signal in the GPS data, which was discussed
 584 in Section 2. Additionally, we see systematic misfit in the later postseismic period west of the
 585 Landers and Hector Mine earthquakes, which may be the result of unmodeled postseismic de-
 586 formation resulting from following those earthquakes. Lastly, there are clear discrepancies be-
 587 tween the observed and predicted vertical deformation displacements following the first year
 588 after the El Mayor-Cucapah earthquake. We observe a broad uplift throughout Southern California,
 589 which is inconsistent with any postseismic model.

593 **4 Discussion**

594 It has long been recognized that deep afterslip and viscoelastic relaxation following an
 595 upper crustal earthquake can result in similar horizontal ground deformation at the surface [e.g.
 596 *Savage*, 1990; *Pollitz et al.*, 2001; *Hearn*, 2003; *Feigl and Thatcher*, 2006]. The similarity of
 597 the horizontal postseismic deformation results in a non-uniqueness in inferences of afterslip
 598 or viscoelastic relaxation. In contrast, the spatial pattern of vertical postseismic deformation
 599 has been proposed to be a discriminant between deep afterslip and viscoelastic relaxation [e.g.
 600 *Pollitz et al.*, 2001; *Hearn*, 2003]. It is, however, important to note that patterns of vertical de-
 601 formation are very sensitive to the depth-dependence of viscosity below the upper crust [*Yang*
 602 and *Toksöz*, 1981; *Hetland and Zhang*, 2014]. The similarity between deformation resulting
 603 from deep afterslip and viscoelastic relaxation of coseismic stresses is different from the ill-
 604 posedness described in Section 3.2. In our method, any inferred afterslip will also mechani-
 605 cally drive additional viscoelastic relaxation. The horizontal deformation resulting from deep
 606 afterslip will generally be in the opposite direction as horizontal deformation resulting from
 607 viscoelastic relaxation of subsequent stresses in the lower crust (Figure 9). As a result, there
 608 is a trade-off between inferences of deep afterslip and lower crustal viscosity. In our synthetic
 609 tests in *Hines and Hetland* [2016], we have found that inverting surface deformation for af-
 610 terslip and viscosity within the same depth interval tends to result in overestimated afterslip
 611 and an underestimated viscosity.

612 Most postseismic studies assume Maxwell viscoelasticity in the lower crust and upper
 613 mantle [e.g. *Nur and Mavko*, 1974; *Pollitz et al.*, 2000; *Hetland*, 2003; *Freed et al.*, 2006; *John-*
 614 *son et al.*, 2009; *Hearn et al.*, 2009], which is the simplest viscoelastic rheologic model. In South-
 615 ern California, postseismic studies following the Landers [*Pollitz et al.*, 2000], Hector Mine
 616 [*Pollitz et al.*, 2001], and El Mayor-Cucapah earthquake [*Spinler et al.*, 2015; *Rollins et al.*, 2015],
 617 have assumed Maxwell viscoelasticity in the lower crust and upper mantle and have inferred
 618 upper mantle viscosities on the order of 10^{17} to 10^{18} Pa s and lower crust viscosities $\gtrsim 10^{19}$
 619 Pa s. These postseismic studies are consistent with *Kaufmann and Amelung* [2000] and *Cav-*
 620 *alié et al.* [2007], who found that an upper mantle viscosity of 10^{18} Pa s and a crustal viscos-
 621 ity $\gtrsim 10^{20}$ Pa s are necessary to describe subsidence resulting from changes in loading from
 622 Lake Mead. This isostatic adjustment is a process with similar spatial and temporal scales as
 623 postseismic deformation, and thus the inferred viscosities of these two types of studies would
 624 likely agree. While these studies found viscosities that are consistent with our effective vis-
 625 cosities from Section 3.2, they are inconsistent with viscosity estimates made from geophys-
 626 ical processes that occur over longer time scales. For example, *Lundgren et al.* [2009] found
 627 that lower crust and upper mantle viscosities on the order of 10^{21} and 10^{19} Pa s, respectively,
 628 are needed to describe interseismic deformation along the Southern San Andreas fault zone
 629 in the Salton Sea region. An even higher mantle viscosity, on the order of 10^{20} Pa s, is re-
 630 quired to describe isostatic adjustment resulting from the draining of Lake Bonneville, which
 631 occurs on the time scales of 10^4 years [*Crittenden*, 1967; *Bills and May*, 1987].

632 An additional deficiency with the Maxwell rheology is that it predicts a steady decay
 633 in the rate of postseismic deformation over time, which fails to describe the commonly ob-
 634 served rapid, early transience followed by a relatively steady rate of postseismic deformation.
 635 One could explain the early transient postseismic deformation with fault creep and the later
 636 phase with relaxation in a Maxwell viscoelastic lower crust and upper mantle [e.g. *Hearn et al.*,
 637 2009; *Johnson et al.*, 2009]. However, postseismic deformation at distances greater than ~ 200
 638 km from the El Mayor-Cucapah epicenter can only be attributed to viscoelastic relaxation [*Freed*
 639 *et al.*, 2007] and we have demonstrated that the far-field deformation cannot be explained with
 640 a Maxwell rheology (Figure ??7).

641 We found that a Zener rheology in the upper mantle with a transient viscosity of $\sim 10^{18}$
 642 Pa s does a noticeably better job at predicting far-field postseismic deformation. A general-
 643 ization of the Zener viscoelastic model, schematically represented as several Kelvin elements
 644 connected in series, is commonly used to describe seismic attenuation [*Liu et al.*, 1976]. The
 645 highest viscosity needed to describe seismic attenuation is on the order of 10^{16} Pa s [*Yuen and*

646 *Peltier*, 1982] which has a characteristic relaxation time on the order of days. Even though
 647 our inferred transient viscosity is orders of magnitude larger than that required for seismic at-
 648 tenuation models, the two models are not incompatible. Rather, the delayed elasticity in seis-
 649 mic attenuation models occurs on such short time scales that it can be considered part of the
 650 instantaneous elastic phase of deformation associated with the preferred Zener model in this
 651 study.

652 Of course, ~~it has long been recognized that~~ a Zener rheology provides an incomplete de-
 653 scriptions of the asthenosphere, as it does not have the fluid-like behavior required to explain
 654 isostatic rebound or convection in the mantle [O'Connell, 1971]. *Yuen and Peltier* [1982] pro-
 655 posed a Burgers rheology with a low transient viscosity ($\eta_K \approx 10^{16}$ Pa s) and high steady-
 656 state viscosity ($\eta_M \approx 10^{21}$ Pa s) to describe both seismic attenuation and long term geologic
 657 processes. The justification of a Burger's rheology mantle is further supported by laboratory
 658 experiments on olivine [Chopra, 1997]. *Pollitz* [2003] sought to describe postseismic defor-
 659 mation following Hector Mine with a Burgers rheology mantle and they found a best fitting
 660 transient viscosity of 1.6×10^{17} Pa s and steady-state viscosity of 4.6×10^{18} Pa s. While
 661 the Burgers rheology was introduced as a means of bridging the gap between relaxation ob-
 662 served in long and short term geophysical processes, the inferred steady state viscosity from
 663 *Pollitz* [2003] is still inconsistent with the Maxwell viscosities inferred from studies on the earth-
 664 quake cycle and Lake Bonneville. The transient viscosity inferred by *Pollitz* [2003] is constrained
 665 by the earliest phase of postseismic deformation following the Hector Mine earthquake. While
 666 *Pollitz* [2003] ruled out deep afterslip as an alternative mechanism based on inconsistent ver-
 667 tical deformation, it is still possible to successfully describe all components of early postseis-
 668 mic deformation following the Hector Mine earthquake with afterslip at seismogenic depths
 669 [Jacobs *et al.*, 2002]. It is then possible that the preferred rheologic model from *Pollitz* [2003]
 670 was biased towards inferring a particularly low transient viscosity by neglecting to account for
 671 afterslip. This is in contrast to the present study, where we have inferred a viscosity structure
 672 simultaneously with afterslip. We also argue that a transient rheology is necessary to explain
 673 postseismic deformation; however, our preferred transient viscosity of $\sim 10^{18}$ Pa s in the up-
 674 per mantle is an order of magnitude larger than the transient viscosity found by *Pollitz* [2003].
 675 The transient viscosity inferred here is consistent with the results of *Pollitz* [2015], who reanalyzed
 676 postseismic data following the Landers and Hector Mine earthquake allowing the first few months
 677 of transient deformation to be described by afterslip. Since a Zener model is able to describe
 678 the available postseismic deformation following the El Mayor-Cucapah earthquake, any Burg-
 679 ers rheology with a steady-state viscosity that is $\gtrsim 10^{20}$ Pa s, effectively infinite over five years,
 680 would also be able to describe the postseismic deformation. Such a Burgers model might then
 681 be consistent with the steady-state viscosities necessary for lake loading, interseismic defor-
 682 mation, and mantle dynamics.

683 5 Conclusion

684 We have extracted a ~~filtered and~~ smoothed estimate of postseismic deformation follow-
 685 ing the El Mayor-Cucapah earthquake from GPS displacement time series. Our estimated post-
 686 seismic deformation reveals far-field (epicentral distances ~~beyond ~200~~ $\gtrsim 200$ km) transient
 687 deformation which is ~~largely~~ undetectable after about three years. Near-field deformation ex-
 688 hibits transience that decays to a sustained, elevated rate after about one or two years. We found
 689 that near-field transient deformation can be explained with shallow afterslip, and the sustained
 690 rate of near-field deformation can either be explained with continued afterslip or viscoelastic
 691 relaxation in the lower crust. Far-field transient deformation can be more definitively ascribed
 692 to viscoelastic relaxation at depths greater than ~ 60 km. Beneath that depth, a transient vis-
 693 cosity of $\sim 10^{18}$ $\sim 1 \times 10^{18}$ Pa s is required to describe the rate of far-field deformation through-
 694 out the five years considered in this study. By describing the available postseismic defor-
 695 mation with a transient rheology in the mantle, our preferred model does not conflict with the
 696 generally higher steady-state viscosities inferred from geophysical processes occurring over
 697 longer time scales.

698 **Acknowledgements**

699 We thank Andy Freed for an illuminating discussion on the data used in this study. This
 700 material is based on EarthScope Plate Boundary Observatory data services provided by UN-
 701 AVCO through the GAGE Facility with support from the National Science Foundation (NSF)
 702 and National Aeronautics and Space Administration (NASA) under NSF Cooperative Agree-
 703 ment No. EAR-1261833. The data used in this study can be found at www.unavco.org. This
 704 material is based upon work supported by the National Science Foundation under Grant Num-
 705 bers EAR 1045372 and EAR 1245263.

706 **References**

- 707 Aagaard, B. T., M. G. Knepley, and C. A. Williams (2013). A domain decomposition
 708 approach to implementing fault slip in finite-element models of quasi-static and dy-
 709 namic crustal deformation, *Journal of Geophysical Research: Solid Earth*, 118, doi:
 710 10.1002/jgrb.50217.
- 711 Argus, D. F., M. B. Heflin, G. Peltzer, F. Crampé, and F. H. Webb (2005), Interseismic
 712 strain accumulation and anthropogenic motion in metropolitan Los Angeles, *Journal of*
 713 *Geophysical Research: Solid Earth*, 110(4), 1–26, doi:10.1029/2003JB002934.
- 714 Aster, R. C., B. Borchers, and C. H. Thurber (2011), Parameter Estimation and Inverse
 715 Problems, vol. 90, Academic Press.
- 716 Bawden, G. W., W. Thatcher, R. S. Stein, K. W. Hudnut, and G. Peltzer (2001), Tectonic
 717 contraction across Los Angeles after removal of groundwater pumping effects., *Nature*,
 718 412(August), 812–815, doi:10.1038/35090558.
- 719 Bills, B. G., and G. M. May (1987), Lake Bonneville: Constraints on Lithospheric Thick-
 720 ness and Upper Mantle Viscosity From Isostatic Warping of Bonneville, Provo, and
 721 Gilbert Stage Shorelines, *Journal of Geophysical Research-Solid Earth and Planets*,
 722 92(B11), 11,493–11,508, doi:10.1029/JB092iB11p11493.
- 723 Çakir, Z., S. Ergintav, H. Özener, U. Dogan, A. M. Akoglu, M. Meghraoui, and
 724 R. Reilinger (2012), Onset of aseismic creep on major strike-slip faults, *Geology*,
 725 40(12), 1115–1118, doi:10.1130/G33522.1.
- 726 Cavalié, O., M. P. Doin, C. Lasserre, and P. Briole (2007), Ground motion measurement in
 727 the Lake Mead area, Nevada, by differential synthetic aperture radar interferometry time
 728 series analysis: Probing the lithosphere rheological structure, *Journal of Geophysical*
 729 *Research: Solid Earth*, 112(3), 1–18, doi:10.1029/2006JB004344.
- 730 Cetin, E., Z. Çakir, M. Meghraoui, S. Ergintav, and A. M. Akoglu (2014), Extent and
 731 distribution of aseismic slip on the İsmetpaşa segment of the North Anatolian Fault
 732 (Turkey) from Persistent Scatterer InSAR, *Geochemistry, Geophysics, Geosystems*, 15,
 733 doi:10.1002/2014GC005307. Received.
- 734 Chopra, P. N. (1997), High-temperature transient creep in olivine rocks, *Tectonophysics*,
 735 279, 93–111, doi:10.1016/S0040-1951(97)00134-0.
- 736 Crittenden, M. (1967), Viscosity and Finite Strength of the Mantle as Determined from
 737 Water and Ice Loads*, *Geophysical Journal of the Royal Astronomical ...*, pp. 261–279,
 738 doi:10.1111/j.1365-246X.1967.tb06243.x.
- 739 Davis, J. L., B. P. Wernicke, and M. E. Tamisiea (2012), On seasonal signals in geode-
 740 tic time series, *Journal of Geophysical Research: Solid Earth*, 117(1), 1–10, doi:
 741 10.1029/2011JB008690.
- 742 Feigl, K. L., and W. Thatcher (2006), Geodetic observations of post-seismic transients in
 743 the context of the earthquake deformation cycle, *Comptes Rendus - Geoscience*, 338,
 744 1012–1028, doi:10.1016/j.crte.2006.06.006.
- 745 Fletcher, J. M., O. J. Teran, T. K. Rockwell, M. E. Osokin, K. W. Hudnut, K. J. Mueller,
 746 R. M. Spelz, S. O. Akciz, E. Masana, G. Faneros, E. J. Fielding, S. Leprince, A. E.
 747 Morelan, J. Stock, D. K. Lynch, A. J. Elliott, P. Gold, J. Liu-Zeng, A. González-
 748 Ortega, A. Hinojosa-Corona, and J. González-García (2014), Assembly of a large

- 749 earthquake from a complex fault system: Surface rupture kinematics of the 4 April
 750 2010 El Mayor-Cucapah (Mexico) Mw 7.2 earthquake, *Geosphere*, 10(4), 797–827,
 751 doi:10.1130/GES00933.1.
- 752 Freed, A. M., R. Bürgmann, E. Calais, J. Freymueller, and S. Hreinsdóttir (2006), Impli-
 753 cations of deformation following the 2002 Denali, Alaska, earthquake for postseismic
 754 relaxation processes and lithospheric rheology, *Journal of Geophysical Research: Solid*
 755 *Earth*, 111, 1–23, doi:10.1029/2005JB003894.
- 756 Freed, A. M., R. Bürgmann, and T. Herring (2007), Far-reaching transient motions after
 757 Mojave earthquakes require broad mantle flow beneath a strong crust, *Geophysical*
 758 *Research Letters*, 34, 1–5, doi:10.1029/2007GL030959.
- 759 Gonzalez-Ortega, A., Y. Fialko, D. Sandwell, F. A. Nava-pichardo, J. Fletcher,
 760 J. Gonzalez-garcia, B. Lipovsky, M. Floyd, and G. Funning (2014), El Mayor-
 761 Cucapah (Mw7.2) earthquake: early near-field postseismic deformation from In-
 762 Sar and GPS observations, *Journal of Geophysical Research*, 119, 1482–1497, doi:
 763 10.1002/2013JB010193.Received.
- 764 Hauksson, E., J. Stock, K. Hutton, W. Yang, J. A. Vidal-Villegas, and H. Kanamori
 765 (2011), The 2010 Mw 7.2 El mayor-cucapah earthquake sequence, Baja Califor-
 766 nia, Mexico and Southernmost California, USA: Active seismotectonics along the
 767 Mexican pacific margin, *Pure and Applied Geophysics*, 168(3918), 1255–1277, doi:
 768 10.1007/s00024-010-0209-7.
- 769 Hearn, E. H. (2003), What can GPS data tell us about the dynamics of post-seismic defor-
 770 mation ?, (2003), 753–777.
- 771 Hearn, E. H., S. McClusky, S. Ergintav, and R. E. Reilinger (2009), Izmit earthquake post-
 772 seismic deformation and dynamics of the North Anatolian Fault Zone, *Journal of Geo-
 773 physical Research: Solid Earth*, 114(August 2008), 1–21, doi:10.1029/2008JB006026.
- 774 Hetland, E. A. (2003), Postseismic relaxation across the Central Nevada Seismic Belt,
 775 *Journal of Geophysical Research*, 108(Figure 2), 1–13, doi:10.1029/2002JB002257.
- 776 Hetland, E. A., and G. Zhang (2014), Effect of shear zones on post-seismic deformation
 777 with application to the 1997 Mw 7.6 manyi earthquake, *Geophysical Journal Interna-
 778 tional*, 198, 259–269, doi:10.1093/gji/ggu127.
- 779 Hines, T. T., and E. A. Hetland (2013), Bias in estimates of lithosphere viscosity from
 780 interseismic deformation, *Geophysical Research Letters*, 40(16), 4260–4265, doi:
 781 10.1002/grl.50839.
- 782 Hines, T. T., and E. A. Hetland (2016), Rapid and simultaneous estimation of fault slip
 783 and heterogeneous lithospheric viscosity from post-seismic deformation, *Geophysical*
 784 *Journal International*, 204(1), 569–582, doi:10.1093/gji/ggv477.
- 785 Jacobs, A., D. Sandwell, Y. Fialko, and L. Sichoux (2002), The 1999 (Mw7.1) Hector
 786 Mine, California, Earthquake: Near-Field Postseismic Deformation from ERS Interfer-
 787 ometry, *Bulletin of the Seismological Society of America*, 92(May), 1433–1442.
- 788 Johnson, K. M., and P. Segall (2004), Viscoelastic earthquake cycle models with deep
 789 stress-driven creep along the San Andreas fault system, *Journal of Geophysical Re-
 790 searchB: Solid Earth*, 109, 1–19, doi:10.1029/2004JB003096.
- 791 Johnson, K. M., R. Bürgmann, and J. T. Freymueller (2009), Coupled afterslip and vis-
 792 coelastic flow following the 2002 Denali Fault, Alaska earthquake, *Geophysical Journal*
 793 *International*, 176(3), 670–682, doi:10.1111/j.1365-246X.2008.04029.x.
- 794 Jónsson, S., P. Segall, R. Pedersen, and G. Bjornsson (2003), Post-earthquake ground
 795 movements correlated to pore-pressure transients, *Nature*, 424(July), 179–183, doi:
 796 10.1038/nature01758.1.
- 797 Kaufmann, G., and F. Amelung (2000), Reservoir-induced deformation and continental
 798 rheology in vicinity of Lake Mead, Nevada, *Journal of Geophysical Research*, 105(B7),
 799 16,341, doi:10.1029/2000JB900079.
- 800 Kroll, K. A., E. S. Cochran, K. B. Richards-Dinger, and D. F. Sumy (2013), Aftershocks
 801 of the 2010 Mw 7.2 El Mayor-Cucapah earthquake reveal complex faulting in the Yuha
 802 Desert, California, *Journal of Geophysical Research: Solid Earth*, 118(October), 6146–

- 6164, doi:10.1002/2013JB010529.
- Lekic, V., S. W. French, and K. M. Fischer (2011), Lithospheric Thinning Beneath Rifted Regions of Southern California, *Science*, 334(November), 783–787.
- Liu, H.-P., D. L. Anderson, and H. Kanamori (1976), Velocity dispersion due to anelasticity; implications for seismology and mantle composition, *Geophysical Journal International*, 47(1), 41–58, doi:10.1111/j.1365-246X.1976.tb01261.x.
- Lundgren, P., E. A. Hetland, Z. Liu, and E. J. Fielding (2009), Southern San Andreas-San Jacinto fault system slip rates estimated from earthquake cycle models constrained by GPS and interferometric synthetic aperture radar observations, *Journal of Geophysical Research: Solid Earth*, 114(2), 1–18, doi:10.1029/2008JB005996.
- McGuire, J. J., and P. Segall (2003), Imaging of aseismic fault slip transients recorded by dense geodetic networks, *Geophysical Journal International*, 155(3), 778–788, doi:10.1111/j.1365-246X.2003.02022.x.
- Meade, B. J., and B. H. Hager (2005), Block models of crustal motion in southern California constrained by GPS measurements, *Journal of Geophysical Research B: Solid Earth*, 110, 1–19, doi:10.1029/2004JB003209.
- Murray, J. R., and P. Segall (2005), Spatiotemporal evolution of a transient slip event on the San Andreas fault near Parkfield, California, *Journal of Geophysical Research : Solid Earth*, 110(9), 1–12, doi:10.1029/2005JB003651.
- Nur, A., and G. Mavko (1974), Postseismic viscoelastic rebound, *Science*, 183(4121), 204–206, doi:10.1038/098448b0.
- O'Connell, R. J. (1971), Rheology of the Mantle, *EOS, Transactions, American Geophysical Union*, 52, 140–142.
- Osokin, M. E., J. R. Arrowsmith, A. Hinojosa Corona, A. J. Elliott, J. M. Fletcher, E. J. Fielding, P. O. Gold, J. J. Gonzalez Garcia, K. W. Hudnut, J. Liu-Zeng, and O. J. Teran (2012), Near-field deformation from the El Mayor-Cucapah earthquake revealed by differential LIDAR, *Science*, 335(6069), 702–705, doi:10.1126/science.1213778.
- Pollitz, F., C. Wicks, and W. Thatcher (2001), Mantle Flow Beneath a Continental Strike-Slip Fault : Postseismic Deformation After the 1999 Hector Mine Earthquake, *Science*, 1814(2001), 1814–1818, doi:10.1126/science.1061361.
- Pollitz, F. F. (2003), Transient rheology of the uppermost mantle beneath the Mojave Desert, California, *Earth and Planetary Science Letters*, 215, 89–104, doi:10.1016/S0012-821X(03)00432-1.
- Pollitz, F. F., G. Peltzer, and R. Bürgmann (2000), Mobility of continental mantle: Evidence from postseismic geodetic observations following the 1992 Landers earthquake, *Journal of Geophysical Research*, 105(1999), 8035, doi:10.1029/1999JB900380.
- Pollitz, F. F., R. Bürgmann, and W. Thatcher (2012), Illumination of rheological mantle heterogeneity by the M7.2 2010 El Mayor-Cucapah earthquake, *Geochemistry, Geophysics, Geosystems*, 13(6), 1–17, doi:10.1029/2012GC004139.
- Pollitz, F. F. (2015). Postearthquake relaxation evidence for laterally variable viscoelastic structure and water content in the Southern California mantle, *Journal of Geophysical Research: Solid Earth*, 120, 2672–2696. doi:10.1002/2014JB011603.
- Rauch, H. E., F. Tung, and C. T. Striebel (1965), Maximum likelihood estimates of linear dynamic systems, *AIAA Journal*, 3(8), 1445–1450.
- Riva, R. E. M., and R. Govers (2009), Relating viscosities from postseismic relaxation to a realistic viscosity structure for the lithosphere, *Geophysical Journal International*, 176, 614–624, doi:10.1111/j.1365-246X.2008.04004.x.
- Rollins, C., S. Barbot, and J.-P. Avouac (2015), Postseismic Deformation Following the 2010 M7.2 El Mayor-Cucapah Earthquake : Observations , Kinematic Inversions , and Dynamic Models, *Pure and Applied Geophysics*, doi:10.1007/s00024-014-1005-6.
- Savage, J. C. (1990), Equivalent strike-slip earthquake cycles in half-space and lithosphere-asthenosphere earth models, *Journal of Geophysical Research*, 95, 4873, doi:10.1029/JB095iB04p04873.

- 856 Savage, J. C., and J. L. Svarc (2009), Postseismic relaxation following the 1992 M 7.3
857 Landers and 1999 M 7.1 Hector Mine earthquakes , southern California, *Journal of*
858 *Geophysical Research*, 114(B01401), doi:10.1029/2008JB005938.
- 859 Savage, J. C., J. L. Svarc, and S. B. Yu (2005), Postseismic relaxation and transient creep,
860 *Journal of Geophysical Research: Solid Earth*, 110, 1–14, doi:10.1029/2005JB003687.
- 861 Segall, P., and M. Mathews (1997), Time dependent inversion of geodetic data, *Journal of*
862 *Geophysical Research*, 102.
- 863 Spinler, J. C., R. A. Bennett, C. Walls, L. Shawn, and J. J. G. Garcia (2015), As-
864 sessing long-term postseismic deformation following the M7.2 4 April 2010, El
865 Mayor-Cucapah earthquake with implications for lithospheric rheology in the
866 Salton Trough, *Journal of Geophysical Research: Solid Earth*, 120, 3664–3679, doi:
867 10.1002/2014JB011613.Received.
- 868 Wei, M., D. Sandwell, Y. Fialko, and R. Bilham (2011a), Slip on faults in the Imperial
869 Valley triggered by the 4 April 2010 Mw 7.2 El Mayor-Cucapah earthquake revealed by
870 InSAR, *Geophysical Research Letters*, 38(January), 1–6, doi:10.1029/2010GL045235.
- 871 Wei, M., Y. Liu, Y. Kaneko, J. J. McGuire, and R. Bilham (2015), Dynamic triggering of
872 creep events in the Salton Trough, Southern California by regional M5.4 earthquakes
873 constrained by geodetic observations and numerical simulations, *Earth and Planetary
874 Science Letters*, 427, 1–10, doi:10.1016/j.epsl.2015.06.044.
- 875 Wei, S., E. Fielding, S. Leprince, A. Sladen, J.-P. Avouac, D. Helmberger, E. Hauksson,
876 R. Chu, M. Simons, K. Hudnut, T. Herring, and R. Briggs (2011b), Superficial sim-
877 plicity of the 2010 El MayorCucapah earthquake of Baja California in Mexico, *Nature
878 Geoscience*, 4(9), 615–618, doi:10.1038/ngeo1213.
- 879 Yang M., and M. N. Toksöz (1981), Time-dependent deformation and stress relaxation
880 after strike-slip earthquakes, *Journal of Geophysical Research*, 86, 2889–2901.
- 881 Yuen, D. A., and W. R. Peltier (1982), Normal modes of the viscoelastic earth, *Geo-
882 physical Journal of the Royal Astronomical Society*, 69, 495–526, doi:10.1111/j.1365-
883 246X.1982.tb04962.x.